

Copyright © 1983, by the author(s).
All rights reserved.

Permission to make digital or hard copies of all or part of this work for personal or classroom use is granted without fee provided that copies are not made or distributed for profit or commercial advantage and that copies bear this notice and the full citation on the first page. To copy otherwise, to republish, to post on servers or to redistribute to lists, requires prior specific permission.

THE COMPLETE DYNAMICS OF THE FORCED
JOSEPHSON JUNCTION CIRCUIT:
THE REGIONS OF CHAOS

by

F. M. A. Salam and S. S. Sastry

Memorandum No. UCB/ERL M83/69

1 October 1983

ELECTRONICS RESEARCH LABORATORY

College of Engineering
University of California, Berkeley
94720

The Complete Dynamics of the Forced Josephson
Junction Circuit: The Regions of Chaos

by

F. M. A. Salam and S. S. Sastry*

Department of Mechanical
Engineering and Mechanics
Systems Group
Drexel University
Philadelphia, PA 19104

Department of Electrical
Engineering and Computer Sciences
University of California
Berkeley, CA 96720

*Research supported by a Regents Junior Faculty Fellowship, June-July 1983,
and by the Joint Services Electronics Program contract F49620-79-C-0178.

The authors are thankful to Jerrold Marsden of the department of Mathematics,
University of California, Berkeley, for helpful discussions.

Abstract

We treat the complete dynamics of the Josephson junction circuit with both d.c. and a.c. current forcing, with emphasis on the a.c. case. Specifically, we derive analytically the complete bifurcation diagram of the a.c. forced Josephson junction. We thus place on analytic grounds the qualitative, experimental and simulation work of Belykh, Pedersen and Soerensen; specially that which pertains to the regions of chaos. Combining previous results from the literature with our new results, we provide a comprehensive picture of the total dynamics of the a.c. forced case; as well as smooth insightful transitions to the associated I-V characteristics. Explicit asymptotic formulae for the curves that separate the different regions in the bifurcation diagram are also given.

Section 1. Introduction

We focus on the dynamics of the Josephson junction circuit with both d.c. and a.c. forcing, with emphasis on the a.c. case. Specifically, we derive analytically the complete bifurcation diagram of the a.c. forced Josephson junction, as well as the associated I-V characteristic. We place on firm analytic grounds the qualitative, experimental, and simulation work of Belykh, Pedersen and Soerensen [7], specially that which pertains to regions of chaos—the work of [7] is the most thorough to date. Abidi and Chua [3], Odyniec and Chua [13, 14] supplied analytic treatment to when the Josephson junction possesses periodic (rotational) orbits. We utilize their results, as well as ours, to provide a comprehensive picture of the total dynamics of the a.c. forced case; and smooth insightful transitions to the associated I-V characteristics.

The key to realizing the afore mentioned program of obtaining the a.c. bifurcation diagram is to prove analytically the existence of chaos, for certain parameter values, in the dynamics of the a.c. forced junction. Chaos, i.e. complex orbital behavior, occurs in many systems of practical interest. In addition to a huge volume of simulation evidence, chaos has been analytically shown to exist, for instance, in the Duffing equations (Greenspan and Holmes [8]), the swing equations of a power system (Kopell and Washburn [12], Salam, Marsden and Varaiya [2]). It would appear superficially that the results presented in [2] (evidence of the Arnold diffusion variety of chaos) which are valid for system equations associated with the dynamics of forced pendulums, can readily be transcribed to the present case. Certainly the dynamics of the forced junction are those of a forced pendulum. The difference, however, lies in the fact that the damping associated with these dynamics (their departure from being Hamiltonian) is not necessarily small--this necessitates several non-trivial modifications in the theory presented in [10, 9, 1, 2]. We prove the existence of 'Smale horseshoe' chaos in the dynamics of the Josephson junction using the method of

Melnikov thereby validating the experimental and simulation result of [6, 7, 11] in the 10-300 GHz range. We use our results to obtain the complete bifurcation diagram of the a.c. forced junction.

The outline of our paper and our contributions are as follows: In Section 2 we review the model of the Josephson junction dynamics. We briefly review the bifurcation diagram of the d.c. forced junction derived in [3,5,7,17] as well as the I-V characteristic of the d.c. forced junction. We then explain the a.c. bifurcation diagram of [7] on the grounds of simulation, experiment and qualitative arguments. We describe the region of the a.c. dynamics which has been studied by Chua and Odyniec in [13, 14]—they explain essentially the piecewise constant portion of the I-V characteristic in the a.c. forced junction.

We point out in Section 2, the need for analytic proofs for the existence of chaos in certain parameter ranges to analytically confirm the conjecture of [7]. To this end, we begin with a brief discussion of chaos and the Melnikov technique for establishing the presence of a Smale-Birkhoff horseshoe in the dynamics of a periodically forced nonlinear system. We do not review the results on the specifics of the chaos associated with the horseshoe here—the reader is referred to the papers of Kopell and Washburn [12], Salam, Marsden and Varaiya [1], Greenspan and Holmes [8], Holmes [10], and the new book of Guckenheimer and Holmes [9] for this. In Sections 4 and 5 we apply these techniques to establish the existence of chaos in the junction for different sets of parameter ranges—Section 4 deals with junctions with low conductance values; whereas Section 5 has no such restriction.

We point out here that the treatment of chaos, as it applies to the Josephson junction, was attempted in [14]. The case of large conductance, corresponding to Section 5 here, was only treated qualitatively as in [7]. The attempt to use the Melnikov technique for the low conductance case (with also a zero constant current), corresponding to a special case of Section 4 here, was technically incorrect, for failure to show the following: the improper (Melnikov) integrals obtained exist and are finite; and further

they do not equal zero simultaneously. Only in the event that these integrals can be evaluated explicitly, that these technical questions can be directly checked. These points will be clarified in the context of Section 4.

In Section 6, we collect all the results to analytically derive the complete a.c. bifurcation diagram of the junction and the relation between the a.c. and d.c. bifurcation diagram. We close the section with a discussion of the effect on our analysis of increasing the amplitude of the a.c. forcing of the junction beyond its 'very small' value.

For a good description of recent advances in superconducting devices and circuits see Van Duzer and Turner [16]. Further, the presence of chaos in the junction dynamics results in increased noise observed at the junction as discussed in [6, 7, 11]. This is particularly of consequence when the junction is used in mixer applications.

Section 2 Dynamics of the Josephson Junction

2.1 The Model

The dynamics of a Josephson junction driven by a current source as shown in Fig. 1 (see e.g. [3, 6, 7, 11, 13, 16]) satisfies the following differential equation:

$$\frac{hC}{4\pi e} \frac{d^2\phi}{dt^2} + \frac{hG}{4\pi e} \frac{d\phi}{dt} + I_0 \sin\phi = i_s(t) \quad (2.1)$$

Here h is Planck's constant, e the electronic charge, I_0 a threshold current associated with the tunnelling current, C the junction capacitance, G the junction conductance and ϕ the difference in phase of the order parameters across the junction. The junction voltage v is given by

$$v = \frac{h}{4\pi e} \frac{d\phi}{dt} \quad (2.2)$$

(2.1) may be rescaled so as to make it dimensionless as follows: set $\tau = \frac{4\pi e I_0}{hG} t$,

$$\beta = \frac{4\pi e I_0}{h} \frac{C}{G^2} \text{ and } \bar{i}_s(\tau) = \frac{1}{I_0} i_s\left(\frac{hG}{4\pi e I_0} \tau\right). \text{ Their equation (2.1) reads as}$$

$$\beta \ddot{\phi} + \dot{\phi} + \sin\phi = \bar{i}_s(\tau) \quad (2.3)$$

with $\dot{\phi} = \frac{d\phi}{d\tau}$, $\ddot{\phi} = \frac{d^2\phi}{dt^2}$. The form of the scaling (2.3) is not standard (it is degenerate

when $G = 0$). Sometimes an alternate scaling of (2.1) is useful. Define

$$\tau = \left(\frac{4\pi e I_0}{hC}\right)^{\frac{1}{2}} t; \quad d = \left(\frac{h}{4\pi e I_0 C}\right)^{\frac{1}{2}} G; \quad \text{and } i'_s(\tau) = \frac{1}{I_0} i_s\left(\left(\frac{hC}{4\pi e I_0}\right)^{\frac{1}{2}} \tau\right) \text{ to obtain}$$

$$\ddot{\phi} + d\dot{\phi} + \sin\phi = i'_s(\tau) \quad (2.4)$$

(this scaling is degenerate when $C = 0$). The form (2.4) is useful in some contexts since d has the physical interpretation of damping. Note that β of (2.3) is equal to $1/d^2$ in (2.4). We will use both models (2.3) and (2.4) as convenient.

2.2 Constant Forcing (DC Analysis)

Equation (2.3) has been studied extensively in the instance that $\bar{i}_s(\tau) = \rho$,

(equivalently, $i_s(t) = I_{dc}$), as the equation by Andronov, Khaiken, and Vitt [4],

Belykh, Pedersen and Soerensen [7], Abidi and Chua [3], Odyneic and Chua [13] and in the context of the swing equations of a power system by Arapostathis, Sastry and Varaiya [5]. We review the results briefly: rewriting (2.3) with $\dot{\phi} = y$ and $\dot{i}_s(\tau) = \rho$ as a first order system we have

$$\dot{\phi} = y, \dot{y} = \frac{-y - \sin\phi + \rho}{\beta} \quad (2.5)$$

Equation (2.5) is periodic in ϕ . Consequently, the state (ϕ, y) can be viewed either as an element of $1R \times 1R$ or $S^1 \times 1R$ where $S^1 = [0, 2\pi]$ with $0, 2\pi$ identified. The state space $S^1 \times 1R$ is more natural, but we use both $1R \times 1R$ and $S^1 \times 1R$ as per convenience.

2.2.1 Bifurcation Diagram for the DC Excited Junction

The bifurcation diagram of (2.5) with ρ, β as parameters is shown in Figure 2 (for $\beta \geq 0$). The diagram is symmetric about the β -axis so that we will discuss it only for positive values of β . In the region (a), equation (2.5) has two equilibrium points in $S^1 \times 1R$; the one a node and the other a saddle. All trajectories converge to one or the other equilibrium point as shown in Figure 3(a). In the region (c), (2.5) has two equilibrium points and a stable periodic orbit on $S^1 \times 1R$. As shown in Fig. 3(c), the stable periodic orbit on $S^1 \times 1R$ corresponds to an unbounded trajectory on $1R \times 1R$ - such a periodic orbit is known as a rotation. A trajectory that forms a periodic orbit both on $S^1 \times 1R$ and on $1R \times 1R$ is referred to simply as an oscillation to distinguish it from a rotation. In the region (f) (2.5) has only a stable periodic orbit - a rotation, see Figure 3f. The curves separating regions (a), (c) and (f) are the bifurcation curves - (b) : $= \{(\rho, \beta) : \rho = \rho_c(\beta), \beta > \beta_0\}$, (d) : $= \{(\rho, \beta) : \rho = 1, \beta > \beta_0\}$ and (e) : $= \{(\rho, \beta) : \rho = 1, \beta \leq \beta_0\}$. On (b), the phase portrait of (2.5) includes two equilibrium points and a saddle connection as shown in Figure 3b. On (d), the phase portrait includes a single equilibrium point obtained by the fusion of the saddle and the node (a saddle-node bifurcation) and a rotation as shown in Figure 3d. On the surface (e), the saddle node and saddle connection occur simultaneously as shown in Figure 3e. Note that

the curves (b), (d) and (e) join smoothly at β_0 .

The sequence of bifurcations obtained when ρ is increased for a fixed value of β is illustrated by the two horizontal lines (A) and (B) in Figure 2. Line (B) corresponds to a small value of β (consequently, large damping d) and line (A) to an intermediate value of β . Traversing line (A) in the direction of increasing ρ starting from $\rho = 0$, one successively obtains the phase portraits shown in Figures 3(a), 3(b), 3(c), 3(d), and 3(f). Traversing line (B) in the direction of increasing ρ , one obtains the phase portraits of Figures 3(a), 3(e) and 3(f). We utilize these lines in our discussion of the I-V characteristics of the junction.

2.22 I-V Characteristics of the DC-Excited Junction

While the bifurcation diagram of Figure 2 gives the complete portrait of the dynamics, one is often interested for applications in an I-V characteristic i.e., a plot of I_{dc} (proportional to ρ , specifically $I_{dc} = I_0 \rho$) vs. V_{av} (proportional to the time averaged value of $y = \frac{d\phi}{dc}$, specifically $\frac{h}{2\pi e} < \frac{d\phi}{dt} >$). Figure 4 gives two such plots: 4(a) and (b) corresponding respectively to the junction with intermediate and low values of β . We explain Figure 4 in the context of our bifurcation diagram (Figure 2) and the phase portraits in Figure 3.

Consider first a junction which has an intermediate value of β , say, β at line (A) in the bifurcation diagram of Figure 2. We study the V_{av} vs. I_{dc} curve as I_{dc} (or equivalently ρ) is gradually (quasistatically) increased from zero, i.e., we traverse the line (A) in the bifurcation diagram. Initially, we are in region (a); all trajectories converge to one of the two equilibrium points on $S^1 \times 1R^1$. Since, $y = 0$ at each of these points (of course, it is extremely unlikely that the trajectory will converge to the saddle equilibrium point); the steady state value of the voltage V , or $V_{av} = 0$. When ρ increases above the value $\rho_c(\beta)$, we are in region (c), where there is both a rotation and two equilibrium points on $S^1 \times 1R^1$. However, in the experiment that is being performed (increasing I_{dc} gradually), the initial conditions for the system (2.5) will be (with a positive measure) in the domain of attraction of the stable equilibrium point and consequently, the trajectory will

converge to the steady state value of zero. (This positive measure is related to the relative size of the region of attraction of the stable equilibrium point. It approaches a zero-measure, i.e., the region of attraction of the stable equilibrium approaches zero area, as ρ approaches 1.) Finally, when ρ exceeds 1; the equilibria annihilate each other in a saddle-node leaving only the stable rotation. All trajectories then converge to the rotation (in region (f)) where the average value of y , i.e., V_{av} , $\neq 0$. This explains the jump in the characteristic of Figure 4(a). In this figure, we show the jump occurring at $I_{dc} = I_o$ (i.e., $\rho=1$), though, in an actual experiment, the jump may occur for $I_{dc} < I_o$ and I_{dc} near I_o .

We now explain the hysteresis in the characteristic of Figure 4(a), corresponding to gradually reducing I_{dc} (and ρ) from values of $\rho > 1$ (region (f)) along the horizontal line (A) in Figure 2. As ρ is reduced below 1, the two equilibria reappear; but initial conditions are such as to cause the trajectory to converge (with a positive measure) to the rotation, now in region (c). The positive measure here is the compliment of the one associated with the stable equilibrium. It approaches zero-measure as ρ approaches $\rho_c(\beta)$. At $\rho = \rho_c(\beta)$, the rotation is destroyed in a saddle-node leaving only the equilibria and consequently convergence of all trajectories to points where the average value of $y = 0$. This explains the hysteretic jump in the characteristic at, or before, $I_{dc} = I_{dc}(\beta)$ (i.e., $\rho = \rho_c(\beta)$). We now derive an expression for the non-zero I-V curve:

$$V_{av} = \frac{h}{2\pi e} \left(\frac{1}{T} \int_0^T y \, dt \right) = \frac{h}{2\pi e} \langle y \rangle; \text{ where } T \text{ is the period of the rotation.}$$

From (2.5)

$$\frac{dy}{dt} = -y - \frac{\sin \phi + \rho}{\beta}$$

so that by integrating both sides from 0 to T , we have

$$\langle y \rangle = \rho. \text{ Hence,}$$

$$V_{av} = \frac{h}{2\pi e} \frac{I}{I_o} \quad I > I_{dc}(\beta) \quad (2.6)$$

The diagram of Fig. 4b corresponds to a junction with a fixed low value of $\beta < \beta_0$. Consider again the experiment of gradually increasing ρ (along line(B) in Figure 2). For $\rho < 1$, we are in region(a) and $V_{av} = 0$. For $\rho > 1$, we are in region (f) and V_{av} satisfies equation (2.6). For decreasing ρ ; exactly the opposite takes place and there is no hysteresis--though a jump occurs at $I_{dc} = I_0$. Thus, the simultaneous occurrence of the saddle-node and saddle connection (region(e)) prevents the existence of competing stable steady states, i.e., an equilibrium point and a rotation, which caused the hysteresis in Figure 4a.

2.3 Sinusoidal Forcing (AC Analysis)

This is the case of primary interest to us in this paper, namely, equation (2.3) with $i_s(\tau) = \rho + \epsilon \sin \omega \tau$ (bias + small sinusoidal forcing). It is the model for the dynamics of the Josephson junction when used in microwave generators and mixers [7,13,16]. In standard first order, (2.3) now reads

$$\dot{\phi} = y, \dot{y} = -\frac{y - \sin \phi + \rho + \epsilon \sin \omega \tau}{\beta} \quad (2.7)$$

(2.7) was first studied by Belykh, Pedersen and Soerensen [7]. Their work was thorough but primarily qualitative (i.e., Analytic details are often absent). Abidi and Chua [3] studied analytically the case when $\beta = 0$ (zero junction capacitance) and ϵ not necessarily small--in this case equation (2.3) simplifies to

$$\dot{\phi} = \rho - \sin \phi + \epsilon \sin \omega \tau \quad (2.8)$$

a first order equation periodic in both ϕ and τ and hence considered as a flow on a torus. The rotation number technique was then applied (see Pliss [15]). Odyniec and Chua [13] showed in analytical detail that the conclusions of [3] are valid not only for $\beta = 0$ but also for small β by using perturbation arguments to show that the (stable) invariant torus associated with (2.8) is perturbed to a stable invariant torus (for a sufficiently small β) which attracts trajectories of (2.8). They also treated the case when ϵ is small and β is large so as to satisfy $\beta > \beta_0$ and $\rho > \rho_c(\beta)$. Such a β lies in regions (c) or (f) in the diagram of figure 2,

and hence the phase portrait of the dc forced Josephson junction possesses a stable rotation. Their study was solely to account for the effect that a small nonzero ϵ produces on the stable rotation: using the integral manifold approach one concludes that, for sufficiently small ϵ , the (stable) torus on which the rotation resides, survives to another (stable) torus; on the new torus, one employs the rotation number technique as in [3].

The work of [3, 13] was contained in the work of Belykh et al [7], though the latter treats a slightly more general form of equation (2.7), namely,

$$\dot{\phi} = y, \quad \dot{y} = \frac{1}{\beta} [-(1 + \gamma \cos \phi)y - \sin \phi + \epsilon \sin \omega t] \quad (2.9)$$

While our primary interest is in the instance that $\gamma = 0$ in equation (2.9) we will begin by a description of the qualitative results of [7], which are the most complete to date.

2.3.1 The AC Bifurcation Diagram of Belykh, et al [7]

Figures 5, 6 are reproduced from [7], with the parameter γ in (2.9) assumed non-zero. Figure 5 is a bifurcation diagram in the parameters β, σ (with γ fixed)—a section of the 3-dimensional bifurcation diagram in β, σ, γ . Figure 6 displays topologically different portraits (of the Poincaré map) numbered corresponding to different regions of Figure 5. (Since Figure 5 is symmetric across the β axis, it is drawn only for $\sigma \geq 0$).

To discuss Figures 5 and 6 consider rewriting (2.9) as

$$\begin{aligned} \dot{\phi} &= y \\ \dot{y} &= \frac{1}{\beta} [-(1 + \gamma \cos \phi)y - \sin \phi + \sigma + \epsilon + \sin \theta] \\ \dot{\theta} &= \omega \end{aligned} \quad (2.10)$$

θ is assumed to lie not on $1\mathbb{R}$ but on an interval $[0, 2\pi]$ with 0 and 2π identified i.e. $\theta \in S^1$. Now (2.10) is an autonomous system which is periodic in ϕ, θ (with period 2π). Consider now the map $P(\tau_0): (\phi(\tau_0), y(\tau_0), \theta(\tau_0)) \xrightarrow{\hspace{1cm}} (\phi(\tau_0 + \frac{2\pi}{\omega}), y(\tau_0 + \frac{2\pi}{\omega}), \theta(\tau_0 + \frac{2\pi}{\omega}))$; i.e. in the change in ϕ, y, θ during one period of the

forcing. Since the system (2.10) is autonomous the map $P(\tau_0)$ is the same for all τ_0 . Further since $\theta(\tau_0 + \frac{2\pi}{\omega}) = \theta(\tau_0) \bmod 2\pi$, we need only concentrate on the map $P : (\phi(\tau_0), y(\tau_0)) \rightarrow (\phi(\tau_0 + \frac{2\pi}{\omega}), y(\tau_0 + \frac{2\pi}{\omega}))$ for same τ_0 . This map is referred to as the period-one or Poincaré map. As before we can define the Poincaré map P either from $1R^1 \times 1R^1$ to itself, or $S^1 \times 1R^1$ to itself. The Poincaré map contains all the information about the dynamics of (2.9), e.g. a fixed point of the Poincaré map $P : 1R^1 \times 1R^1$ to itself corresponds to an oscillation of the system (2.9) and a fixed point of the Poincaré map $P : S^1 \times 1R^1$ to itself which is not a fixed point of $P = 1R^1 \times 1R^1$ to itself corresponds to a rotation of the system (2.9). For further discussion of Poincaré maps see, for instance, [9, 10, 1].

We now discuss the bifurcation diagram of Fig. 5 in terms of the map P . Consider first traversing the bifurcation diagram 5 along $\beta = \text{constant}$, on line A. The portrait of the Poincaré map P , though of now as a discrete dynamical system ([9]), in region ① is shown in Fig. 6(1).. On $S^1 \times 1R^1$, the map P has two fixed points, a stable fixed point M^+ and an unstable (saddle) fixed point M^- . These are the only critical elements of P and all initial conditions converge to one or the other of these points. Thus the system (2.9) has only a stable oscillation (corresponding to M^+) and an unstable oscillation (corresponding to M^-). The stable and unstable manifolds of M^- are shown in Figure 6(1). In the region ②, the map still has only two critical points M^+ and M^- on $S^1 \times 1R^1$. However the 'upper' stable and 'upper' unstable manifolds of M^- and its replica intersect each other transversally once (and hence infinitely often). This intersection implies the existence of infinitely many (unstable) periodic orbits for the equation (2.9), referred to as the horse-shoe kind of chaos. (The precise description, physical meaning and interpretation of this kind of chaos is discussed in Section 3, see also [1, 9, 10, 12]). On the boundary from regions ① to ② and regions ② to ③, the intersection between the stable and unstable manifolds of M^- is tangential rather

than transversal (this case is not completely understood, see, however, the book of Guckenheimer and Holmes [9]) Region ③ is associated with the Poincare section of Figure 6(3). It shows a shaded ring shaped region. The ring is an attracting set which contains infinitely many stable steady state solutions. According to [7] little is known about the ring and its dynamics. We will show in Section 6 that this ring is absent when γ in equation (2.9) is equal to zero. In region ④, there are stable and unstable fixed points corresponding to periodic orbits both of the oscillation and rotation type. Figure 6(4) shows two fixed points of the rotation type (R^- and R^+) and two of the oscillation type (M^- and M^+). In region ⑤ there are only periodic orbits of the rotation type. We elaborate on the dynamics in this region:

Figure 6(5) shows the presence of a stable (attracting) invariant curve containing R^- and R^+ . This corresponds to the existence of a two dimensional stable (attracting) invariant surface for (2.9). This surface is periodic in ϕ and θ and so diffeomorphic to a two-torus. The study of orbital behavior on a two dimensional torus is treated through the use of rotation number μ (see Pliss [15]), i.e., the ratio of the number of rotations in ϕ to the number of rotations in θ . As before it is easy to verify that $\langle y \rangle$ is proportional to μ . The rotation number μ is said to be (structurally) stable, if it remains constant for "sufficiently small" variations of the model, specifically in our case ρ . It can be shown [7,13] that the only stable rotation numbers are rational, i.e., $\mu = p/q$; with $p, q \in \mathbb{Z}_+$ - this, of course, corresponds to a periodic solution on the torus. For details see [3,13,7].

The lowest horizontal line B in Figure 5 crosses only two distinct regions ①, ⑤. For large values of β (corresponding to small values in the damping $d = \beta^{-1/2}$ if model (2.7) is used) new regions emerge. Along line C, for small

values of ρ we enter the region ①. Figure 6(0) shows a Poincaré section for this region. It can be envisioned as having both the 'upper' and 'lower' stable and unstable manifolds of the right hand replica of M^- intersecting, transversally, the 'upper' and 'lower' unstable and stable manifolds of the left hand replica of M^- respectively. Note the resemblance to Figure 6(2), as well as the additional feature of transversal intersection of the 'lower' stable and unstable manifolds. Further, within this loop of intersecting manifolds surrounding M^+ there is an alternating sequence of saddles and stable fixed points of the Poincaré map with the manifolds associated with the saddles intersecting each other transversally. This extremely complicated form of horseshoe chaos is explained in Section 4 and Figure 11 (see [9]). We term this chaos as doubly chaotic. This would imply now for larger values of ρ , the presence of more critical elements than in Figures 6(2), (4) corresponding to regions ②, ④. Proceeding along the line C we encounter the regions ②0, ③0 and ④0 which have the same configurations as the portraits of Figures 6(2), (3) and (4) respectively with the added presence of an alternating sequence of stable and saddle fixed points surrounding the stable fixed point as in Figure 6(0). The curves σ_0^- , σ_c^+ , σ_c^- , σ_h separate the regions ①, ②0, ③0, ④0 and ④ respectively.

The following points about the bifurcation diagram of [7] can be made. It is obtained by qualitative means; in particular the existence of the chaotic regions ① and ② is not proven analytically. The regions ④ and ⑤ have been studied analytically in [13,14]. We will, in Sections 4 and 5, establish rigorously the existence and phase portraits of regions ① and ②. Further for the case when $\gamma = 0$, we show that region ③ does not exist.

Using these analytic arguments, we deduce the form of the curves ρ_c^+ , ρ_t , ρ_0 , ρ_h in Section 6.

2.3.2 The I - V Characteristic

As in Section 2.2, the complete dynamical picture enables us to obtain the V_{av} vs. I_{dc} (i.e. bias current) of the a.c. forced junction. Indeed it was through a combination of experiments and simulation that [7] obtained the bifurcation diagram of Figure 5. Figure 7(a), reproduced from [7], shows one such I-V characteristic corresponding to a junction having an intermediate value for β (the line A in Figure 5).

Before we discuss this characteristic, we make some general comments about the V_{av} vs. I_{dc} characteristic. V_{av} is proportional to the time averaged value of y (technically $\frac{1}{T} \int_0^T y dt$ as $T \rightarrow \infty$), in the steady state. When there are several competing critical elements of the system (2.7), the V_{av} observed can correspond to any one of them, depending on their stability, the size of their domain of attraction and more importantly, the choice of initial conditions in the experiment. The experiment that gives rise to Figure 7(a) consists of gradually increasing I_{dc} and measuring V_{av} for a function having an intermediate value of β , i.e., traversing line A of Figure 5 from left to right and then decreasing I_{dc} . Consider first the case of increasing I_{dc} :

In the region (1), almost all initial conditions will converge to the stable oscillation M^+ with time averaged $y = 0$. In the region 2 (i.e., $\rho \geq \rho_c$), we have in addition to the oscillations M^+ and M^- , an infinite number of unstable oscillations corresponding to the transversal intersection of the stable and unstable manifolds of M^- . However, since the initial conditions are close to the stable oscillation of M^+ , with zero average value, we still get $V_{av} = 0$. The same argument explains, $V_{av} = 0$ in the region (3). In region (4),

we have the stable oscillation M^+ as well as a stable rotation R^+ , however, the initial condition causes the junction to stay locked at M^+ with $V_{av} = 0$. In region 5, the oscillations disappear and the circuits lock onto the stable rotation R^+ , with non-zero average value of y (proportional to the rotation number $\mu = p/q$). Now as I_{dc} increases, the voltage stays constant (since the rotation is stable), for small variations in I_{dc} (or ρ) and changes (jumps) in rational steps corresponding to changes in the rotation number. This part of the I-V characteristic is the focus of [3,13,14] shown in Figure 7b as discontinuous and stepwise constant. Further, the heights of the steps are rationally related.

We now consider the case of decreasing I_{dc} . As ρ (I_{dc}) is decreased, we drop from region 5 to region 4; initial conditions will keep the junction locked to a rotation and yield piecewise constant I-V characteristic as in region 5 (note the hysteresis in the $V_{av}-I_{dc}$ characteristic now). Decreasing ρ into region 3, the circuit locks into the ring of solutions shown in Figure 6(3) yielding the unstable $V_{av}-I_{dc}$ characteristic shown hatched in Figure 7(a). In region 2, the chaotic region, the circuit locks into the infinitely many unstable oscillations associated with the transversal intersection of Figure 6(2). Each of these have almost identical non-zero, average voltages. However, since these infinitely many oscillations are unstable and lie close to the domain of attraction of M^+ the circuit could jump to the stable rotation M^+ , resulting in zero V_{av} . At any rate, there is a sharp increase in the amount of perceived noise in the junction in this region. This is particularly deleterious in application of the junction as a mixer. Some authors show the instability of V_{av} values in the chaotic regions 2, as shaded region in the $V_{av}-I_{dc}$ curve as shown in Figure 7c taken from [6].

2.4 Our Contribution

We have discussed in Section 2.3 the qualitative and simulation work of [7] and the limited analytic work of [3,13,14]. In the rest of this paper we prove rigorously those conclusions of [7] that have not been proven in [3,13,14]. The model we consider is (2.7) with $\gamma = 0$. Since the discussion of regions ④ and ⑤ is more or less complete, we focus in the next four sections on regions ①, ② and ③. We establish the existence of Region ① in Section 4, and Region ② in Section 5. We collect the conclusions of these two sections in Section 6, where we also establish that region ③ is absent for $\gamma = 0$, and the connection between the a.c. and d.c. bifurcation diagrams.

We would like to emphasize that with these proofs an essentially complete analytic picture of the dynamics emerges. We start with a brief review of our major technique: the Melnikov Method.

Section 3. Chaos and the Melnikov Method

Chaos is a form of complicated behavior in the dynamics of deterministic non-linear systems. Some varieties of complex behavior are now well understood - aperiodic solutions, Berkhoff-Smale horseshoes, strange attractors, Arnold diffusion, overlapping of resonances, etc. Chaos entails orbital motion which is reminiscent of noise in that it possesses a broadband spectrum. A dynamical system undergoing chaos may simultaneously possess countably infinite numbers of periodic orbits and recurrent motions which are not periodic. These motions emanate from certain regions in the phase space; moreover, they are extremely sensitive to variations in initial conditions. This extreme sensitivity is exhibited in the form of an uncertainty - over time, two initial conditions starting very close may diverge from one another exponentially (see [1,9] for further discussion).

The majority of cases in which chaos has been reported in the literature are based on simulation or intuitive arguments. One specific form of chaos, the Smale horseshoe and its generalization, the Arnold diffusions has shown itself to be well suited to analysis and has been studied in detail [1,8,9,10]. Further, a technique called the Melnikov technique provides an analytic tool for measuring the presence of the horseshoe chaos in certain periodically forced non-linear systems. In ingenuous form, it gives information about the behavior of the perturbed periodic system based on a calculation involving trajectories of the unperturbed system. We review the method:

Consider the system

$$\dot{x} = f(x) + \varepsilon g(x,t) \quad (3.1)$$

where f, g are sufficiently smooth functions; f from \mathbb{R}^2 to \mathbb{R}^2 ; and g from \mathbb{R}^3 to \mathbb{R}^2 is T -periodic in t . The associated unperturbed system is

$$\dot{\bar{x}} = f(\bar{x}) . \quad (3.2)$$

Assume that the system (3.2) possesses a homoclinic orbit. $\bar{x}_0(t)$, i.e., an orbit that connects a saddle equilibrium point x_0 to itself. From [8] it can be shown that for ϵ small enough, the saddle equilibrium point x_0 gets perturbed to a saddle fixed point x_ϵ of the time-T Poincare map of (3.1) as shown in Figure 8. Let the perturbed stable orbit of x_ϵ be denoted $x_\epsilon^s(t, t_0)$ and the perturbed unstable orbit $x_\epsilon^u(t, t_0)$. Then the following Lemmas are proven in [8,9].

Lemma 3.1

$$\dot{x}_\epsilon^u(t, t_0) = \bar{x}_0(t-t_0) + \epsilon x^{lu}(t, t_0) + O(\epsilon^2), \text{ uniformly in } t \text{ for } t \in]-\infty, t_0]$$

$$\dot{x}_\epsilon^s(t, t_0) = \bar{x}_0(t-t_0) + \epsilon x^{ls}(t, t_0) + O(\epsilon^2), \text{ uniformly in } t \text{ for } t \in [t_0, \infty[.$$

Lemma 3.2 (First Variation Equations)

$$\dot{x}^{lu}(t, t_0) = D_x f(\bar{x}_0(t-t_0)) x^{lu}(t, t_0) + g(\bar{x}_0(t-t_0), t) \quad (3.3)$$

for $t \in]-\infty, t_0]$

$$\dot{x}^{ls}(t, t_0) = D_x f(\bar{x}_0(t-t_0)) x^{ls}(t, t_0) + g(\bar{x}_0(t-t_0), t) \quad (3.4)$$

for $t \in [t_0, \infty[.$

The separation between $x_\epsilon^u(t, t_0)$ and $x_\epsilon^s(t, t_0)$ (see Figure 8) is measured by

$$d_\epsilon(t_0) = \frac{f(\bar{x}_0(0)) \wedge [x_\epsilon^u(t_0, t_0) - x_\epsilon^s(t_0, t_0)]}{|f(\bar{x}_0(0))|} \quad (3.5)$$

where \wedge stands for the wedge product. The first variation of the distance

$d_\varepsilon(t_0)$ can be written as

$$d_\varepsilon(t_0) = \frac{\varepsilon M(t_0)}{|f(\bar{x}_0(0))|} + O(\varepsilon^2) \quad (3.6)$$

where $M(t_0)$ is the Melnikov function given by

$$M(t_0) = f(\bar{x}_0(0)) \wedge [x^{lu}(t_0, t_0) - x^{ls}(t_0, t_0)] \quad (3.7)$$

The interest in evaluating the distance between $x_\varepsilon^u(t, t_0)$ and $x_\varepsilon^s(t, t_0)$ arises from the fact that if they intersect transversely once, they intersect each other infinitely often as shown in Figure 9 forming the so-called Smale horseshoe in the dynamics of the Poincare map with countably many unstable orbits of different periods as well as a periodic recurrent orbit. (See [1,9] for a discussion of the Smale horseshoe). This results in a specific kind of chaos in the dynamics referred to as the Smale horseshoe. The Melnikov method evaluates $M(t_0)$, the first variation in the distance $d_\varepsilon(t_0)$ scaled by $|f(\bar{x}_0(0))|$. Consequently if the function $M(t_0)$ has transversal zeros, i.e., if $\exists \tilde{t}_0$ such that

$$M(\tilde{t}_0) = 0 \quad \frac{dM}{dt_0}(\tilde{t}_0) \neq 0$$

it follows that $x_\varepsilon^u(t, t_0)$ and $x_\varepsilon^s(t, t_0)$ intersect transversally once (and hence infinitely often) resulting in the horseshoe chaos. To obtain an expression for $M(t_0)$ we write (3.5) as

$$M(t_0) = \Delta^u(t_0, t_0) - \Delta^s(t_0, t_0) \quad (3.8)$$

where

$$\Delta^u(t_0, t_0) := f(\bar{x}_0(0)) \wedge x^{lu}(t_0, t_0),$$

and $\Delta^s(t_0, t_0) := f(\bar{x}_0(0)) \wedge x^{ls}(t_0, t_0).$

The essence of the Melnikov method is to evaluate the scalar constants $\Delta^u(t_0, t_0)$ and $\Delta^s(t_0, t_0)$ in terms of the given vector fields f and g along the homoclinic orbit (before perturbation). To that end, one defines

$$\Delta^u(t, t_0) := f(\bar{x}_0(t-t_0)) \wedge x^{lu}(t, t_0) \quad \text{for } t \in]-\infty, t_0] \quad (3.9)$$

and $\Delta^s(t, t_0) := f(\bar{x}_0(t-t_0)) \wedge x^{ls}(t, t_0) \quad \text{for } t \in [t_0, \infty[.$ (3.10)

Using (3.3) and (3.4), obtaining (3.8) becomes a final (resp. initial) value problem for the differential equation satisfied by $\Delta^u(t, t_0)$ (resp $\Delta^s(t, t_0)$); namely

$$\begin{aligned} \dot{\Delta}^u(t, t_0) &= \dot{f} \wedge x^{lu} + f \wedge \dot{x}^{lu} \\ &= [\text{trace } D_{\frac{f}{x}}(\bar{x}_0(t-t_0))] \Delta^u + f(\bar{x}_0(t-t_0)) \wedge \\ &\quad g(\bar{x}_0(t-t_0), t) \quad \text{for } t \in]-\infty, t_0] \end{aligned} \quad (3.11)$$

$$\begin{aligned} \dot{\Delta}^s(t, t_0) &= [\text{trace } D_{\frac{f}{x}}(\bar{x}_0(t-t_0))] \Delta^s + f(\bar{x}_0(t-t_0)) \wedge \\ &\quad g(\bar{x}_0(t-t_0), t) \quad \text{for } t \in [t_0, \infty[\end{aligned} \quad (3.12)$$

Equations (3.11) and (3.12) are scalar linear time varying differential equations which can be explicitly integrated to solve the final and initial value problems respectively. The values $\Delta^u(-\infty, t_0)$ and $\Delta^s(t_0, \infty)$ do not appear in the solutions if $\Delta^u(t, t_0)$ approaches zero more rapidly than $\exp\{-\int_{t_0}^t \text{trace } [D_{\frac{f}{x}} f(\bar{x}_0(s-t_0))] ds\}$ as $t \rightarrow -\infty$ and $\Delta^s(t, t_0)$ approaches 0 more

rapidly than $\exp\{-\int_{t_0}^t \text{trace } D_{\bar{x}} f(\bar{x}_0(s-t_0))ds\}$ as $t \rightarrow \infty$.

Under this condition, (the 'exponential convergence' condition, see [1]), we may write, by integrating (3.11) and (3.12) and substituting in (3.8),

$$\begin{aligned} M(t_0) &= \int_{-\infty}^{\infty} f(\bar{x}_0(t)) \wedge g(\bar{x}_0(t), t+t_0) \cdot \\ &\quad \cdot \exp\{-\int_{t_0}^t \text{trace } D_{\frac{f}{x}}[\bar{x}_0(s)]ds\} dt. \end{aligned} \quad (3.13)$$

This is the Melnikov Integral. Note that the exponential convergence condition is significant only when $\text{trace } [D_{\frac{f}{x}}(\bar{x}_0(s))]$ is non-zero. When the unperturbed system is Hamiltonian, $\text{trace } D_{\frac{f}{x}}(\bar{x}_0(s)) \equiv 0$ so that the Melnikov integral of (3.13) is valid without any further conditions, furthermore the Melnikov integral reads

$$M(t_0) = \int_{-\infty}^{\infty} f(\bar{x}_0(t)) \wedge g(\bar{x}_0(t), t+t_0) dt \quad (3.14)$$

Generally speaking the Melnikov technique has been used to establish chaos in periodic perturbations of Hamiltonian systems. In this paper, we will verify the exponential convergence condition in the Josephon junction circuit model of Section 2, in order to use the Melnikov technique for a non-Hamiltonian system in a novel fashion, (Section 5).

Section 4 Chaos in the Josephson Junction Dynamics:
the close to Hamiltonian case.

The form (2.3) of the Josephson junction dynamics has the form of the equations of a damped pendulum, with damping normalized to 1. In this section we will study the Josephson junction equations where the conductance G and the dc forcing I_{dc} are small. The transformation taken of (2.1) to (2.3) is singular in the limit that $G = 0$. Hence, we will use the scaling of equation 2.6, viz.

$$\ddot{\phi} + d \frac{d\phi}{dt} + \sin \phi = i_s'(t) \quad (4.1)$$

$i_s'(t)$ is of the form $\epsilon(\rho + \sin \bar{\omega}t)$ and $d = \epsilon d_0$, where $\bar{\omega} = \frac{\omega}{d}$; and ϵ is a small parameter. We will show that in this form equation (4.1) possesses a Smale horseshoe in its dynamics. The parameter ranges studied in this section correspond to the large β , small ρ part of the bifurcation diagram of Figure 5.

The unperturbed system (for $\epsilon = 0$) is

$$\begin{aligned} \dot{\phi} &= \bar{y} \\ \dot{\bar{y}} &= -\sin \phi \end{aligned} \quad (4.2)$$

(Notation consistent with Section 3). Equations (4.2) are Hamiltonian with (energy) given by

$$H(\bar{y}, \phi) = \left(\frac{\bar{y}^2}{2} - \cos \phi \right). \quad (4.3)$$

There are two saddle connection orbits for this system as shown in Figure 10 labelled Γ^u (upper) and Γ^l (lower): strictly Γ^u and Γ^l are both homoclinic orbits, when we take into account the 2π -periodicity of equation (4.2) in ϕ , i.e., $\phi \in S^1$ rather than \mathbb{R} .

The value of the hamiltonian $H(\bar{y}, \bar{\phi})$ on these orbits is easily seen to be 1 and the orbits given explicitly by

$$\begin{aligned}\bar{v}(t-t_0) &= \pm 2 \operatorname{sech} (t-t_0) \\ (4.4)\end{aligned}$$

$$\bar{\phi}(t-t_0) = \pm 2 \operatorname{arc tan}[\sinh(t-t_0)]$$

where the + sign is for Γ^U and the - sign is for Γ^L . The Melnikov integral (3.14) is specialized to this case to be

$$\begin{aligned}M(t_0) &= \int_{-\infty}^{\infty} \bar{y}(\rho - d_0 \bar{y} + \sin \bar{\omega}(t+t_0)) dt \\ &= \int_{\pm \pi}^{\pm \pi} \rho d\bar{\phi} - d_0 \int_{-\infty}^{\infty} [\pm 2 \operatorname{sech} t]^2 dt \\ &\quad + \left[\int_{-\infty}^{\infty} \pm 2 \operatorname{sech} t \cdot \cos \bar{\omega} t dt \right] \sin \bar{\omega} t_0. \quad (4.5)\end{aligned}$$

(we have used here $\frac{d\bar{\phi}}{dt} = \bar{y}$, and the fact that $\int_{-\infty}^{\infty} \operatorname{sech} t \sin \bar{\omega} t dt = 0$ - integral of an odd function.) Evaluating (4.5) explicitly yields

$$M(t_0) = \pm \rho 2\pi - 8d_0 + [\pi \bar{\omega} \operatorname{sech} \frac{\pi \bar{\omega}}{2}] \cdot \sin \bar{\omega} t_0 \quad (4.6)$$

For Γ^U , the upper homoclinic orbit, the separation

$$M^U(t_0) = 2\pi \rho - 8d_0 + R(\bar{\omega}) \sin \bar{\omega} t_0 \quad (4.7)$$

where $R(\bar{\omega}) := \pi \bar{\omega} \operatorname{sech} \left(\frac{\pi \bar{\omega}}{2} \right) > 0$.

For (4.7) to have a zero, t_0^* we see that it is necessary to have

$$|-2\pi \rho + 8d_0| \leq R(\bar{\omega}). \quad (4.8)$$

It is easy to verify that the zero, t_0^* is transverse when the inequality is strict for all frequencies $\bar{\omega}$.

When (4.8) becomes an equality, the zero t_0^* is nontransverse and this corresponds to the tangential intersection. The frequencies that correspond to this case are $\bar{\omega} = \frac{(1 + 2\pi)\pi}{2 t_0^*}$.

For I_{dc} ($\rho = I_0 \rho$) values satisfying (4.8), the upper homoclinic curve Γ^U breaks up as in Figure 6(2) and hence implies the presence of a horseshoe chaos. Analogously for Γ^L the lower homoclinic orbit the Melnikov function

$$M^L(t_0) = -2\pi\rho - 8d_0 - R(\bar{\omega}) \sin \bar{\omega} t_0. \quad (4.9)$$

For (4.9) to have transversal zeros, it is necessary (and sufficient) to have

$$|2\pi\rho + 8d_0| \leq R(\bar{\omega}) \quad (4.10)$$

and $\bar{\omega} \neq \frac{(2n+1)\pi}{2 t_0}$ as before.

When ρ is such that both (4.8) and (4.10) are simultaneously satisfied for a fixed $\bar{\omega}$, we have the complicated phase portrait of Figure 11 (note that if (4.10) is satisfied, then (4.8) is also satisfied). In addition to the 'doubly chaotic' intersections of the stable and unstable manifolds of the saddle, there is within the loop of intersecting manifolds an alternating sequence of saddles and stable fixed points of the Poincare map with the manifolds associated with the saddles intersecting each other transversally (overlapping of resonances) - a more comprehensive description of this portrait is in, e.g., [9, page 222].

The portrait of Figure (11) persists for a continuum of 'small' ϵ values corresponding to small d (or to relate this to Figure 5 -

large $\beta = d^{-2} = \epsilon^{-2} d_0^{-2}$, we set $\epsilon = 1$, and consider β to be large). The conditions (4.8) and (4.10) enable us to derive the curves ρ_c^- , ρ_c^+ and ρ_0 as follows: Equation (4.8) is rewritten as two separate conditions

$$\beta^{-1/2} \leq \frac{1}{8} [2\pi \rho + R(\bar{\omega})] \quad (4.11a)$$

and

$$\beta^{-1/2} \geq \frac{1}{8} [2\pi \rho - R(\bar{\omega})] \quad (4.11b)$$

Equation (4.11a) is the equation of ρ_c^- and (4.11b) is the equation of ρ_c^+ - explicitly¹

$$\beta \geq \frac{16}{\pi^2} \left| \rho + \frac{R(\bar{\omega})}{2\pi} \right|^{-2} = : \rho_c^- \quad (4.12a)$$

$$\beta \geq \frac{16}{\pi^2} \left| \rho - \frac{R(\bar{\omega})}{2\pi} \right|^{-2} = : \rho_c^+ \quad (4.12b)$$

Since β is assumed positive, ρ_c^+ is defined only for $\rho \geq \frac{R(\bar{\omega})}{2\pi}$ (equation 4.11b), and $\rho_c^+ \rightarrow \infty$ as $\rho \rightarrow \frac{R(\bar{\omega})}{2\pi}$. Further, at $\rho = 0$, $\rho_c^- = \left(\frac{8}{R(\bar{\omega})} \right)^2$. The curves ρ_c^- and ρ_c^+ are plotted in Figure (12). Since the analysis of this section is valid only for large and intermediate values of β , the curves ρ_c^- , ρ_c^+ diverge from those predicted by (4.12) (a) and (b) for smaller values of β . Hence in Figure (12), we have shown the actual curves ρ_c^- , ρ_c^+ (the solid lines) diverge from the curves ρ_c^- , ρ_c^+ of (4.12) (a) and (b) (the dotted lines) for small values of β . The discussion of the onset of chaos in the small β case is in Section 5.

We now derive the expression for the curve ρ_0 corresponding to region (0) - here (4.10) holds, and hence (4.8) does also, and it gives the equation for ρ_0 as follows: rewrite (4.10) as

1 It seems more appropriate to define ρ_c^- and ρ_c^+ to be (analytic) functions of $\beta^{1/2}$, $\beta \neq 0$, from equations (4.11a-b).

$$\beta^{-1/2} \leq \frac{1}{8} [-2\pi\rho + R(\bar{\omega})] \quad (4.13a)$$

$$\beta^{-1/2} \geq \frac{1}{8} [-2\pi\rho - R(\bar{\omega})] . \quad (4.13b)$$

The inequality (4.13b) is useless since the right hand side is negative (for positive ρ) since $R(\bar{\omega}) > 0$. Equation (4.13a) yields

$$\beta \geq \frac{16}{\pi^2} \left(-\rho + \frac{R(\bar{\omega})}{2\pi} \right)^{-2} = : \rho_0 \quad (4.14)$$

Equation (4.14) is defined only for $\rho \leq \frac{R(\bar{\omega})}{2\pi}$ and $\rho_0 \rightarrow \infty$ as $\rho \rightarrow \frac{R(\bar{\omega})}{2\pi}$.

Further at $\rho = 0$, $\rho_0 = \left(\frac{8}{R(\bar{\omega})} \right)^2$, i.e., it coincides with the curve ρ_c^- at $\rho = 0$. The curve ρ_0 is plotted in Figure (12) also.

Thus, we have shown that for intermediate and large β , we have (horse-shoe) chaos for $\beta - \rho$ parameter values between the curves ρ_c^- and ρ_c^+ and 'globally chaotic' for $\beta - \rho$ parameter values above the curve ρ_0^0 . These correspond to the regions identified qualitatively in [7] (see Figure 5) and are labelled in Figure 12. The other curves ρ_h , ρ_p of Figure 5 can also be obtained at least qualitatively, if not explicitly, using the Melnikov technique to obtain conditions (i.e., inequalities) for the occurrence of the resonance of periodic orbits about the stable fixed point of the Poincare section as shown in Figure 6(0) or Figure (11). The usage of the Melnikov technique in the case of resonances is treated in [9], for instance.

Section 5 Chaos in the Josephson Junction Dynamics -
the non-Hamiltonian case

We consider here the model of (2.7) with $\gamma = 0$ and no small parameter assumptions except on the magnitude of the periodic forcing. The unperturbed system with $\epsilon = 0$ is given by

$$\dot{\phi} = \bar{y}, \quad \dot{\bar{y}} = -\frac{\bar{y} - \sin \bar{\phi} + \rho}{\beta}. \quad (5.1)$$

Let $\rho = \rho_c(\beta)$ i.e., the constant forcing is chosen such that the autonomous system has a homoclinic orbit as in Figure 3b. The Melnikov integral in this case is given by

$$M(t_0) = \int_{-\infty}^{\infty} [\bar{y}(t-t_0) \cdot \frac{1}{\beta} \sin \omega t] \exp\left(\frac{t}{\beta}\right) dt. \quad (5.2)$$

(Note that the presence of the term $\exp\left(\frac{t}{\beta}\right)$ necessitates checking the exponential convergence condition of Section 3 - this is done in the Appendix 1). This may be simplified at

$$\begin{aligned} M(t_0) &= \frac{1}{\beta} \left\{ \left[\int_{-\infty}^{\infty} \bar{y}(t) e^{t/\beta} \sin \omega t dt \right] \cos \omega t_0 \right. \\ &\quad \left. + \left[\int_{-\infty}^{\infty} \bar{y}(t) e^{t/\beta} \cos \omega t dt \right] \sin \omega t_0 \right\} \end{aligned} \quad (5.3)$$

If the integrals in the square bracket exist, are finite and are not both zero, then one can easily show that transversal zeros exist (two in each period, $\frac{2\pi}{\omega}$, in t_0) for all but a discrete set of values in ω (i.e., frequencies at which the inequality becomes an equality), see, e.g., Kopell and Washburn [12], Salam, et al [27]). Our task is to show that these integrals do exist and are finite. Consider the integrals:

$$I_1(\omega) := \int_{-\infty}^{\infty} \bar{y}(t) e^{t/\beta} \sin \omega t \, dt \quad \text{and} \quad I_2(\omega) := \int_{-\infty}^{\infty} \bar{y}(t) e^{t/\beta} \cos \omega t \, dt. \quad (5.4)$$

Since $\bar{y}(t)$ is a bounded smooth function with $\bar{y}(t) \rightarrow 0$ as $t \rightarrow \pm \infty$, it is enough to show that $\bar{y}(t)e^{t/\beta} \rightarrow 0$ fast enough as $t \rightarrow \pm \infty$ for the integrals (5.4) to be finite. Now $\bar{y}(t)$ is a component of $\bar{x}_0(t)$ the homoclinic orbit of the unperturbed system. Hence for t values close to $\pm \infty$, the rate of approach of $\bar{y}(t)$ to the saddle x_0 is given by the eigenvalues of the linearization of the vector field of the unperturbed system close to the saddle equilibrium $x_0 = (\bar{\phi}_0, 0)$ i.e., the eigenvalues of

$$\begin{bmatrix} 0 & 1 \\ -\frac{1}{\beta} \cos \bar{\phi}_0 & -\frac{1}{\beta} \end{bmatrix} \quad (5.5)$$

where $\bar{\phi}_0$ satisfies $\rho = \sin \bar{\phi}_0$. The eigenvalues of (5.5) are respectively

$$\begin{aligned} \lambda^s &= -\frac{1}{2\beta} - \frac{1}{2} \left[\left(\frac{1}{\beta} \right)^2 + 4(1 - \rho^2)^{1/2} \right] < -\frac{1}{\beta} < 0 \\ \lambda^u &= -\frac{1}{2\beta} + \frac{1}{2} \left[\left(\frac{1}{\beta} \right)^2 + 4(1 - \rho^2)^{1/2} \right]^{-1/2} > 0 \end{aligned} \quad (5.6)$$

where λ^s is the negative (stable eigenvalue and λ^u the positive (unstable) eigenvalue of the saddle equilibrium point x_0 . As $t \rightarrow \infty$, $\bar{y}(t)$ approaches 0 as $e^{\lambda^s t}$; while as $t \rightarrow -\infty$ $\bar{y}(t)$ approaches 0 as $e^{\lambda^u t}$. Thus the quantity $\bar{y}(t)e^{t/\beta}$ is of the order of $e^{(\lambda^s + 1/\beta)t}$ as $t \rightarrow \infty$ and of the order of $e^{(\lambda^u + 1/\beta)t}$ as $t \rightarrow -\infty$. From (5.6) it follows that $\bar{y}(t)e^{t/\beta}$ goes to zero exponentially as $t \rightarrow \pm \infty$. Hence the integrals in (5.4) are well defined and finite. The Melnikov integral of (5.3) is thus well defined. The only thing that needs to be shown is that $I_1(\omega)$ and $I_2(\omega)$ are not both zero at all but discretely many frequencies. This follows from the analyticity of the

two integrals in ω . Precisely, $I_2(\omega) + iI_1(\omega)$ is the Fourier transform (an analytic function of ω) of a function $\bar{y}(t)e^{t/\beta}$ which is not identically zero (for all t), see [12]. We have thus shown that the Melnikov integral

$$M(t_0) = \frac{1}{\beta} [I_1(\omega)\cos \omega t_0 + I_2(\omega)\sin \omega t_0]$$

has transversal zeros (two in every period) at all but a discrete set of ω 's. Two difficulties were overcome in using the Melnikov approach in this case (low β case): (1) The validity of the formula for $M(t_0)$ has to be verified by verifying the exponential convergence condition (Appendix), (2) The convergence of the specific improper integral (5.2) has to be verified and then examined for transversal zeros. Such questions must be addressed in any application of the Melnikov integrals. (Only question (2) arises in the Hamiltonian case). We have shown the presence of the horseshoe chaos for $\rho = \rho_c(\beta)$. Since the horseshoe is structurally stable, chaos persists for small variations in ρ and β about $\{(\beta, \rho) : \rho = \rho_c(\beta), \beta \geq \beta_0\}$. The curve ρ_c is shown dotted in Figure 12 relative to ρ_c^- , ρ_c^+ ; and as expected it lies between ρ_c^- and ρ_c^+ . For large values of β the analysis of Section 4 established chaos. For smaller values of β close to β_0 ; one can only say that a neighborhood of the curve ρ_c exhibits the horseshoe chaos and the boundaries of chaotic region ② differ appreciably from the ρ_c^- and ρ_c^+ of 4.12a and 4.12b. We expect that the neighborhood of the curve ρ_c where chaos is encountered shrinks as $\beta \rightarrow \beta_0$. Since smaller values of β (large values of damping d) increase the rate of convergence of trajectories starting off the saddle connection (of the unperturbed system) to the stable equilibrium point (below the saddle connection), see Figure 3b.

Section 6. Conclusions: Transition from the d.c. to the a.c. bifurcation diagram

In this section we combine the results of Sections 4 and 5 with those of [3, 13, 14] to establish the transition from the d.c. to the a.c. bifurcation diagram. To do so, we compare equation (2.5) the (dc-forced model) and (2.10) with $\gamma=0$ (the ac-forced model). Since (2.5) is only two dimensional we augment it with $\dot{\theta}=\omega$ with $\theta \in S^1$ as in (2.10) - this augmentation is called suspension of (2.5). It is equivalent to assuming that the autonomous system is periodic with arbitrary period. Phase portraits of the suspended system (2.5) consist of the (ϕ, y) portraits of Fig. 3 replicated identically for all $\theta \in S^1$. As before period-one or Poincaré maps for the augmented autonomous system can be defined.

We study the transition from the d.c. bifurcation along line (A) of figure 2, to line A of Figure 5. For low values of ρ , we are in region(a) of Figure 2 corresponding to one stable equilibrium point and one saddle (both hyperbolic). Under small periodic perturbation (ϵ small) it is elementary (see [9]) to show that the stable equilibrium point changes to a stable oscillation and the saddle equilibrium to a saddle oscillation (both hyperbolic). The average value of y on both these orbits is zero. (Corresponding to zero average voltage in the steady state).

For $\rho > \rho_c(\beta)$ a stable (hyperbolic) rotation appears in the d.c. dynamics both in the interior of regions(c) and(f) as shown in Figure 3c and 3f. For the augmented dynamics of (2.5) with $(\phi, y, \theta) \in S^1 \times \mathbb{R} \times S^1$ this rotation appears as a stable (hyperbolic) two-dimensional invariant surface diffeomorphic to a two torus. Applying sufficiently small periodic perturbation (ϵ small) to the augmented dynamics (equivalently equation (2.10) with $\gamma=0$), only deforms this invariant surface diffeomorphically (it is, in turn, diffeomorphic to a two torus,

i.e., it is periodic in ϕ and θ). As studied in [13, 14] trajectories on this perturbed torus are conveniently studied using rotation numbers of orbits on the torus, and as discussed in Section 2.3.2. The structurally stable orbits are those corresponding to a rational rotation number $\mu = p/q$ (and is also attracting), see [13]. The average voltage is proportional to these rational numbers (as evidenced by the step-wise I-V characteristic of Figure 7b). When the rotation number μ is not rational the periodic orbits are unstable or non-existent. For these rotation numbers, any one of a set of average voltages may be observed in an experiment - in figure 7(a); from [7], a single diagonal line connecting the steps was observed; in Figure 7(b) of [13], which is obtained theoretically, nothing is filled in between steps; and in Figure 7(c) of [6] the space between steps is shown shaded. This situation corresponds to regions 4 and 5 of Figure (12).

For $\rho = \rho_c(\beta)$ and small or intermediate values of β , the d.c. dynamics show a saddle connection, Figure 3(b). We have shown how small periodic perturbations of this saddle connection result in the presence of the (horseshoe) chaos in Section 5, and the appearance of region 2 in Figure (12).

For β large and ρ small, the d.c. dynamics are near the Hamiltonian that has the phase portrait of Figure 10. We showed how small periodic perturbation of this case results in the appearance of regions 0, 20, 40 in Section 4, we derived analytic expressions for ρ_c^- , ρ_c^+ and ρ_o also. The geometric picture is that the periodic perturbation "splits" the curve $\rho_c(\beta)$ of Figure 2 into the curves ρ_c^- and ρ_c^+ , allowing the region of chaos to emerge as shown in Figure (12).

Region (d) of the d.c. dynamics corresponding to $\rho=1$ translates to a saddle-node bifurcation of the stable and saddle oscillations of the a.c. forced system.

Finally, we consider region (e) of the d.c. dynamics corresponding to the simultaneous saddle connection and saddle-node bifurcations ($\rho=1$, $\beta=\beta_o$). First for $\beta=0$, the system (2.7) reduces to a two-dimensional system which exhibits no

complicated behavior - and using singular perturbation theory [13] it is readily verified that this behavior persists for $\beta < \beta_s < \beta_0$. Thus, the saddle-node of the d.c. dynamics translates to a saddle-node of 'oscillations' in the a.c. dynamics: and the emergence of a 'limit cycle' by saddle connection translates to the corresponding behavior in the a.c. dynamics. The region $\beta_s \leq \beta \leq \beta_0$ is not susceptible to easy analysis by the Melnikov technique since the saddle connection involves non-hyperbolic equilibrium points. We conjecture that since the curves ρ_c^- , ρ_c^+ start off as analytic functions² of ρ (see (4.12)(a)and(b)), they should extend to part of the component of region c as shown dotted in Figure (12).

This completes the transcription of the d.c. bifurcation diagram of Figure 2 to the a.c. bifurcation diagram of Figure 12; since every one of the regions(a)-(f) was studied under periodic perturbation. The transcription is exhaustive and the region of the "ring" 3 of Figure 5 did not appear. We thus conclude that the ring does not exist for $\gamma=0$, (and of course for γ small - since our conclusions are all structurally stable).

Finally we state the following extensions in the form of two remarks. First; the qualitative, simulation and experiments based, study of Belykh, Pedersen and Soerensen [7], as well as of [6] and [11], gives the range of the periodic perturbation parameter ϵ which extends to (comparatively) large values - at these values the analytic tools available all become invalid. However, the physics literature contains numerous experimental and simulation studies which show that properties such as chaos persists and "strengthen" as ϵ extends beyond its analytic range (see [18]). This experimental work had focused on near Hamiltonian Systems and chaos generated by nonanalytic ϵ is referred to as "Strong Stochasticity", where as for analytic ϵ the term "Weak Stochasticity" is used. It is reasonable to believe that chaos "strengthens" for larger ϵ ; since the restriction on the analytic ϵ is primarily to ensure the validity of the measuring technique, namely, the Melnikov method.

2 Analytic functions of β , $\beta \neq 0$; see footnote 1.

The second remark concerns the applicability of our results to power systems; namely, the 3-machine case as in Kopell and Washburn [12], and also in Salam, Marsden, and Varaiya [2]. In [12], the power system model is transformed to one that is identical to model (2.4), with damping d set to zero and $\frac{1}{s}(\tau) = \rho + \epsilon \sin(\bar{\omega}\tau)$ - Hamiltonian. The authors concluded the presence of chaos in this Hamiltonian system, then they offered qualitative arguments to allow the chaotic dynamics to survive the addition of small (positive) damping d . Our result of section 5 supports, in an analytic rigor, their qualitative arguments; moreover it allows for larger amount of damping.

Appendix 1 Existence of the Melnikov Integral (5.2)

Recall that

$$\Delta^u(t, t_0) = f(\bar{x}_0(t-t_0)) \wedge x^{lu}(t, t_0)$$

Since x^{lu} satisfies a(bounded) linear time varying differential equation, i.e.,

$$\dot{x}^{lu}(t, t_0) = \begin{bmatrix} 0 & 1 \\ -\frac{1}{\beta} \cos \bar{\phi}_0(t) & -\frac{1}{\beta} \end{bmatrix} x^{lu}(t, t_0) + \begin{bmatrix} 0 \\ \frac{1}{\beta} \sin \omega t \end{bmatrix}$$

we have that $x^{lu}(t, t_0)$ is bounded for $t \in]-\infty, t_0]$. On the other hand, $f(\bar{x}_0(t-t_0))$ tends exponentially to zero at the rate of $\exp(\lambda^u t)$ as $t \rightarrow \infty$, where $\lambda^u > 0$ is the 'unstable' eigenvalue of the saddle defined in equation (5.6). Further trace $Df_{x_0}(\bar{x}_0(t)) \equiv -\frac{1}{\beta}$ so that $\Delta^u(t, t_0) \exp(-t/\beta)$ tends exponentially to zero as $t \rightarrow \infty$.

Similarly, note that

$$\Delta^s(t, t_0) = f(\bar{x}_0(t - t_0)) \wedge x^{ls}(t, t_0)$$

with $x^{ls}(t, t_0)$ bounded on $[t_0, \infty[$. Further, $f(\bar{x}_0(t - t_0))$ tends exponentially to zero at the rate of $\exp(\lambda^s t)$ as $t \rightarrow \infty$, where $\lambda^s < -\frac{1}{\beta}$, is the 'stable' eigenvalue of the saddle defined in equation (5.6). Hence, $\Delta^s(t, t_0) \exp(-\frac{t}{\beta})$ tends exponentially to zero as $t \rightarrow \infty$.

This establishes the exponential convergence condition of Section 3, and validates the formula (5.2).

References

- [1] F.M. A. Salam, J. Marsden and P. Varaiya, "Chaos and Arnold Diffusion in Dynamical System", IEEE Trans. on Circuits and Systems, Vol CAS-30, September 1983.
- [2] F.M. A. Salam, J. Marsden and P. Varaiya, "Arnold Diffusion in the Swing Equations in a Power System", UCB ERL Memo. M83/13, University of California, Berkeley, March 1983.
- [3] A.A. Abidi and L.O. Chua "On the dynamics of Josephson junction circuits", Electronic Circuits and Systems, Vol. 3 (1979) pp. 186-200
- [4] A.A. Andronov, S.E. Khaiken and A.A. Vitt, Theory of Oscillators, Pergamon, New York (1966).
- [5] A.Arapostathis, S.Sastry and P.Varaiya, "Global Analysis of Swing Dynamics", IEEE Trans on Circuits and Systems, Vol. CAS 29 (1982), pp. 673-679
- [6] E. Ben-Jacobi, I.Goldhirsch, Y. Imry and S. Fishman, "Intermittent chaos in Josephson junctions", Physical Review Letters, Vol. 49 (1982), pp 1599-1602
- [7] V.N. Belykh, N.F. Pedersen and O.H. Soerensen, "Shunted Josephson - junction model I - The Autonomous case and II. The non-autonomous case", Physical Review B, Vol. 16 (1977), pp. 4853-4871.
- [8] B.O. Greenspan and P.J. Holmes, "Homoclinic Orbits, Subharmonics and Global Bifurcation in Forced Oscillations", in Nonlinear Dynamics and Turbulence, ed. G Barenblatt, Pitman (1983)
- [9] J. Guckenheimer and P. J. Holmes, Nonlinear Oscillations, Dynamical Systems and Bifurcations of Vector fields, Applied Mathematical Sciences, No. 42, Springer-Verlag 1983.
- [10] P.J. Holmes, "Averaging and Chaotic Motions in Forced Oscillations", SIAM J. on Appl. Math - Vol. 38 pp. 68-80, and Vol. 40, pp. 167-168, 1980.

- [11] B.A. Huberman, J.P. Crutchfield and N.H. Packard, "Noise Phenomena in Josephson junctions", Applied Physics Letters, Vol. 37 (1980) pp. 750-752.
- [12] N.Kopell and R.B. Washburn, "Chaotic Motion in the Two-Degree-of-Freedom Swing Equations", "IEEE Trans. on Circuits and Systems, Vol. CAS-29 (1982) pp. 738-746.
- [13] M.Odyniec and L.O. Chua, "Josephson-Junction Circuit Analysis via Integral Manifolds", "IEEE Trans. on Circuits and Systems, Vol. CAS-30 (5), May 1983.
- [14] M. Odyniec and L.O. Chua, "Josephson-Junction Circuit Analysis via Integral Manifolds: Part II", "Memo. UCB/ERL M83/12, University of California, Berkeley, March 1983.
- [15] V.A. Pliss, Nonlocal problems of the theory of Oscillations, Academic Press (1966).
- [16] T. Van Duzer and C.W. Turner, Principles of Superconductive Devices and Circuits, Elsevier, New York (1981).
- [17] M. Levi, C. Hoppensteadt, and W.L. Miranker, "Dynamics of the Josephson Junction", Quarterly of Applied Math., July 1978, pp. 167-198.
- [18] A.J. Lichtenberg, and M.A. Lieberman, Regular and Stochastic Motion, Applied Math. Sciences Vol. 38, Springer-Verlag (December 1982).

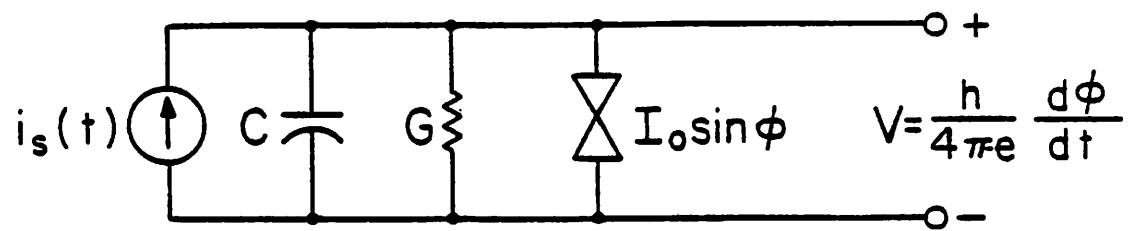


Figure 1. Josephson junction circuit model

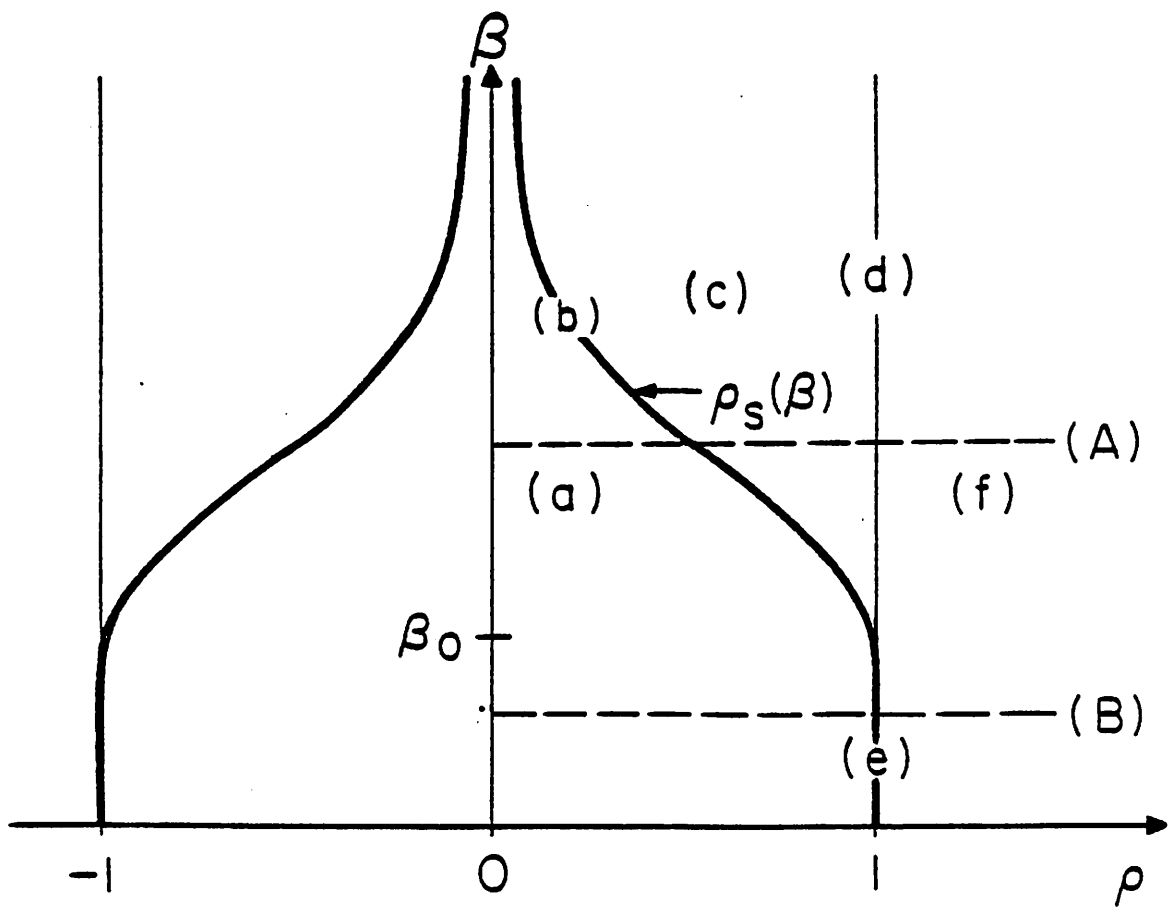


Figure 2. Bifurcation diagram for (2.5)

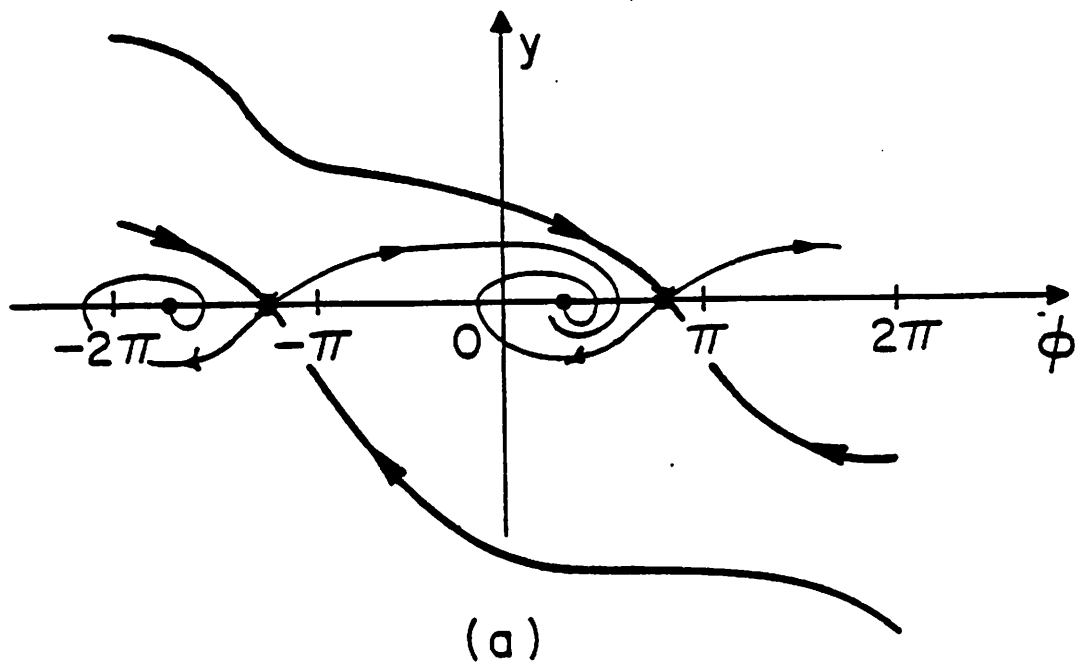


Figure 3a. The completely stable case

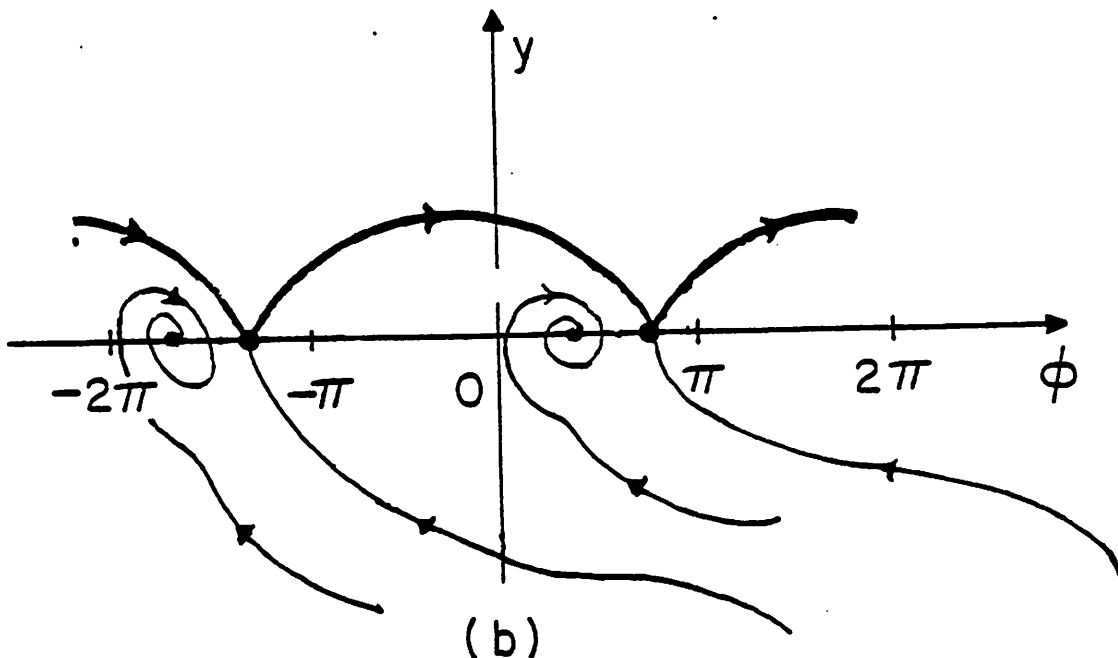


Figure 3b. The saddle connection bifurcation

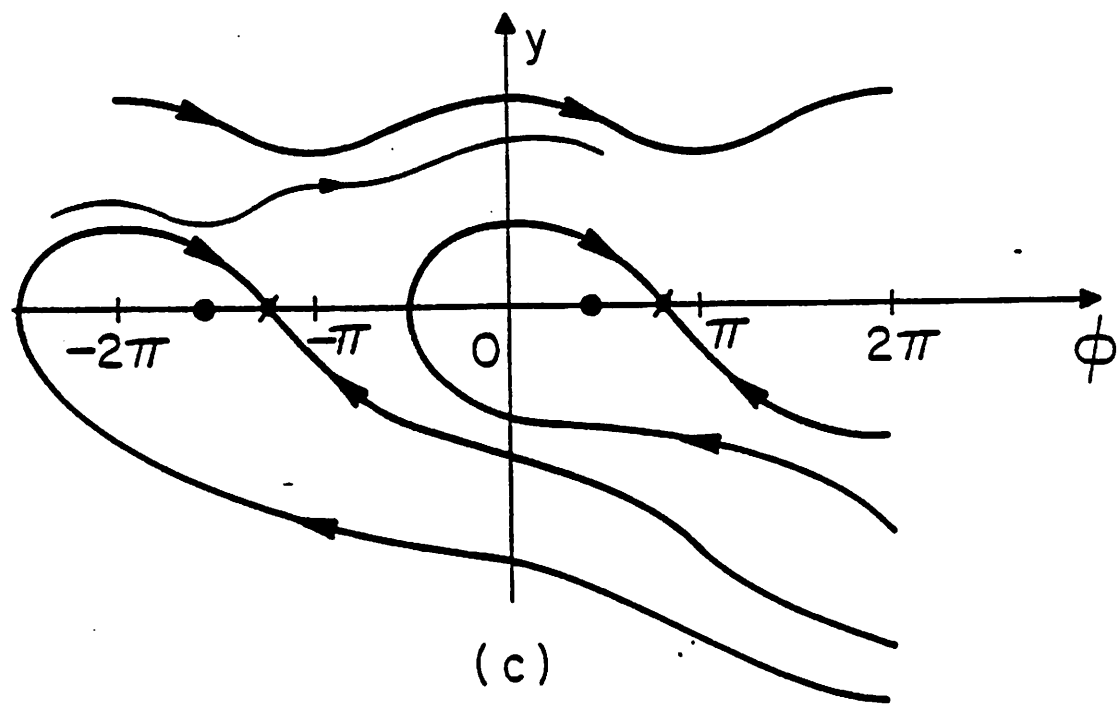


Figure 3c. One stable rotation and two equilibrium points

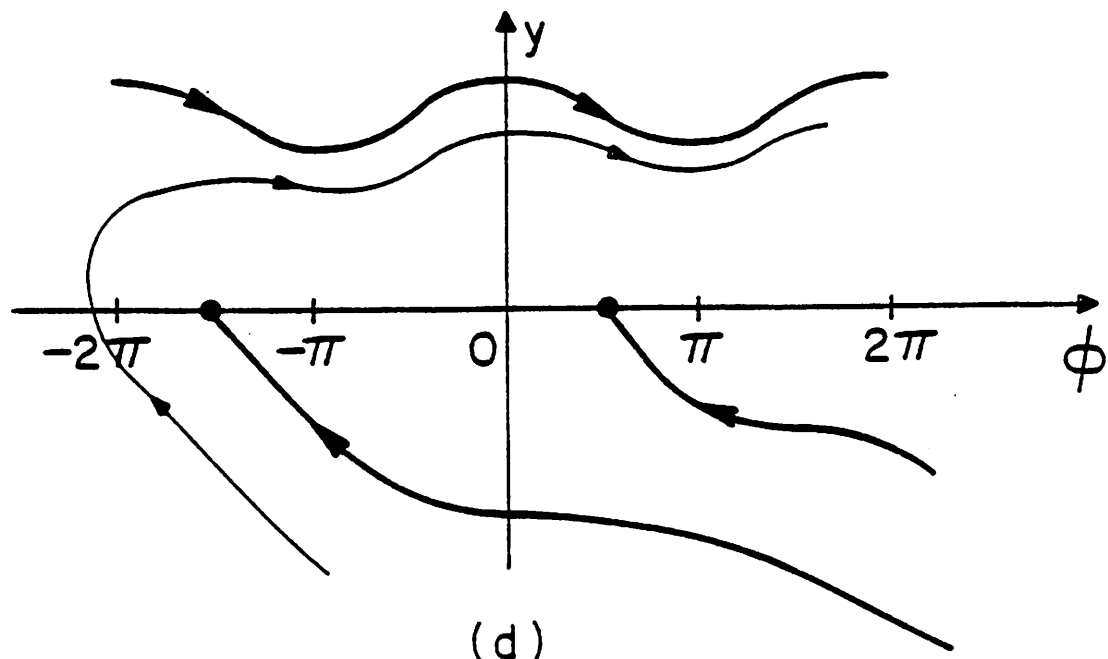


Figure 3d. Saddle-node bifurcation

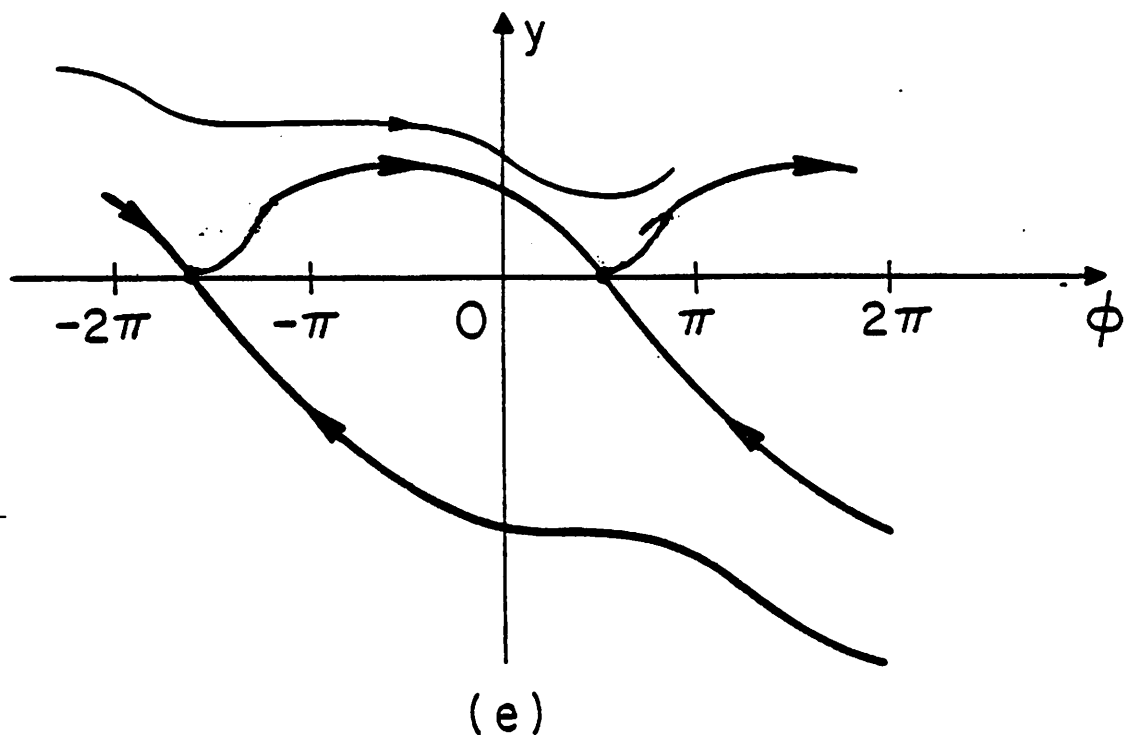


Figure 3e. Simultaneous saddle-node and saddle connection bifurcation

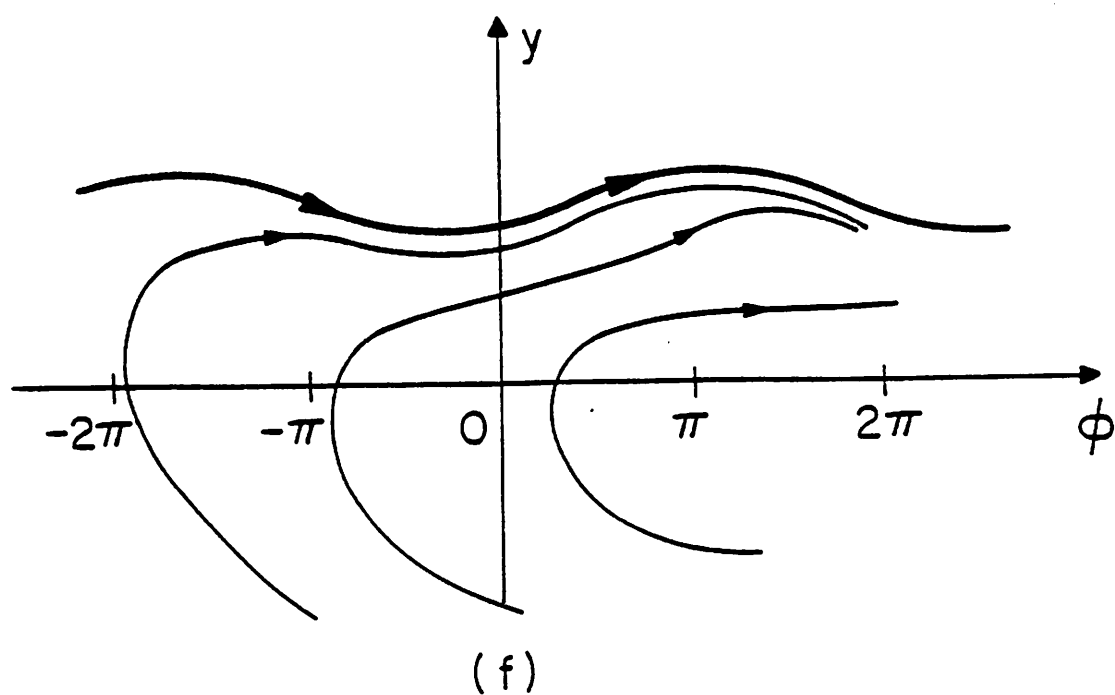


Figure 3f. Single rotation and no equilibrium points.

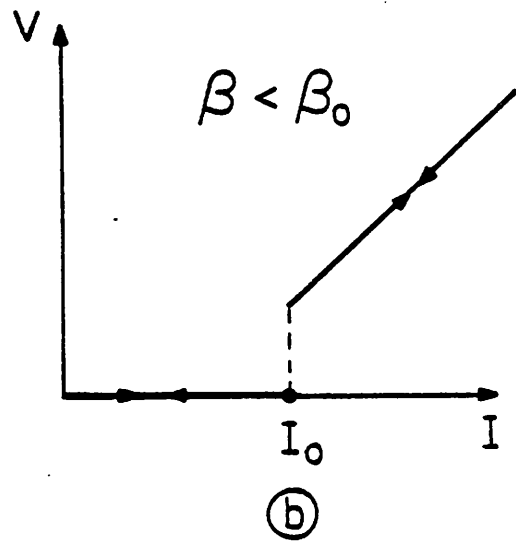
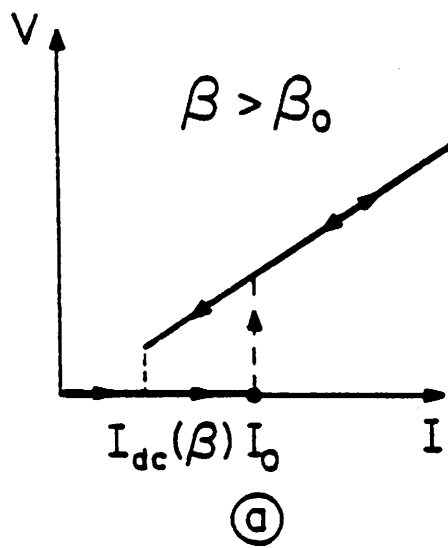


Figure 4. I-V characteristics of the Josephson junction: (a) hysteresis curve corresponding to line (A) in the bifurcation diagram of Figure 2. (b) no hysteresis curve corresponding to line (B) of Figure 2.

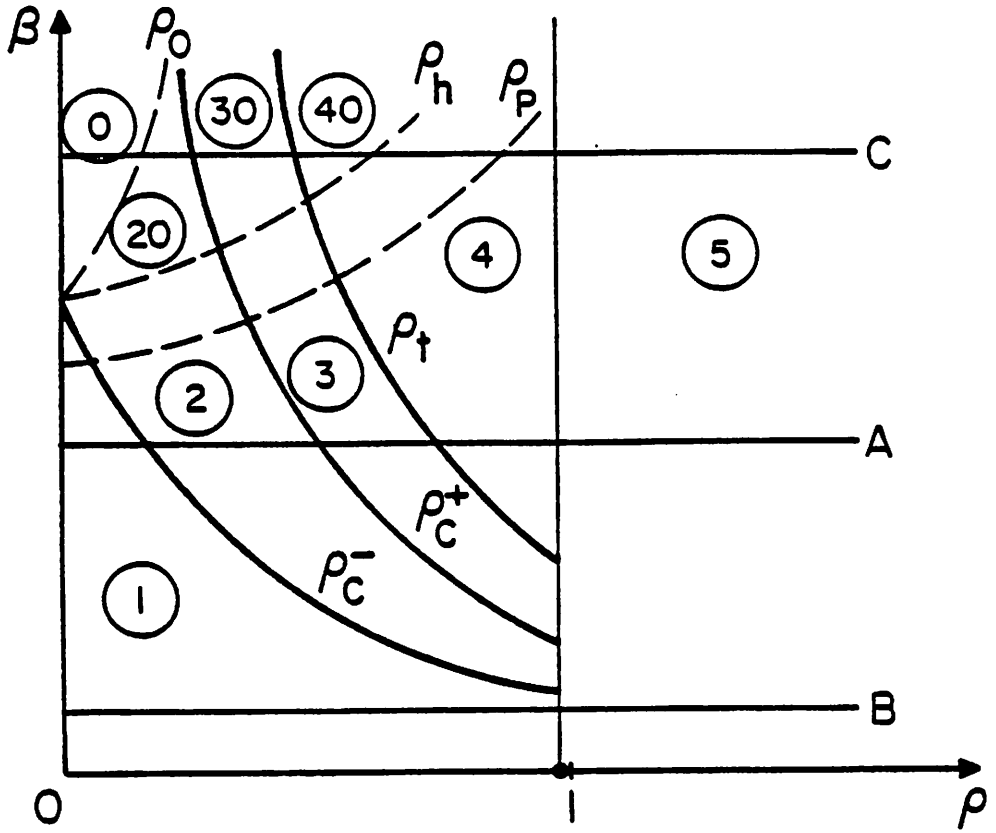


Figure 5. Ac bifurcation diagram of [7]

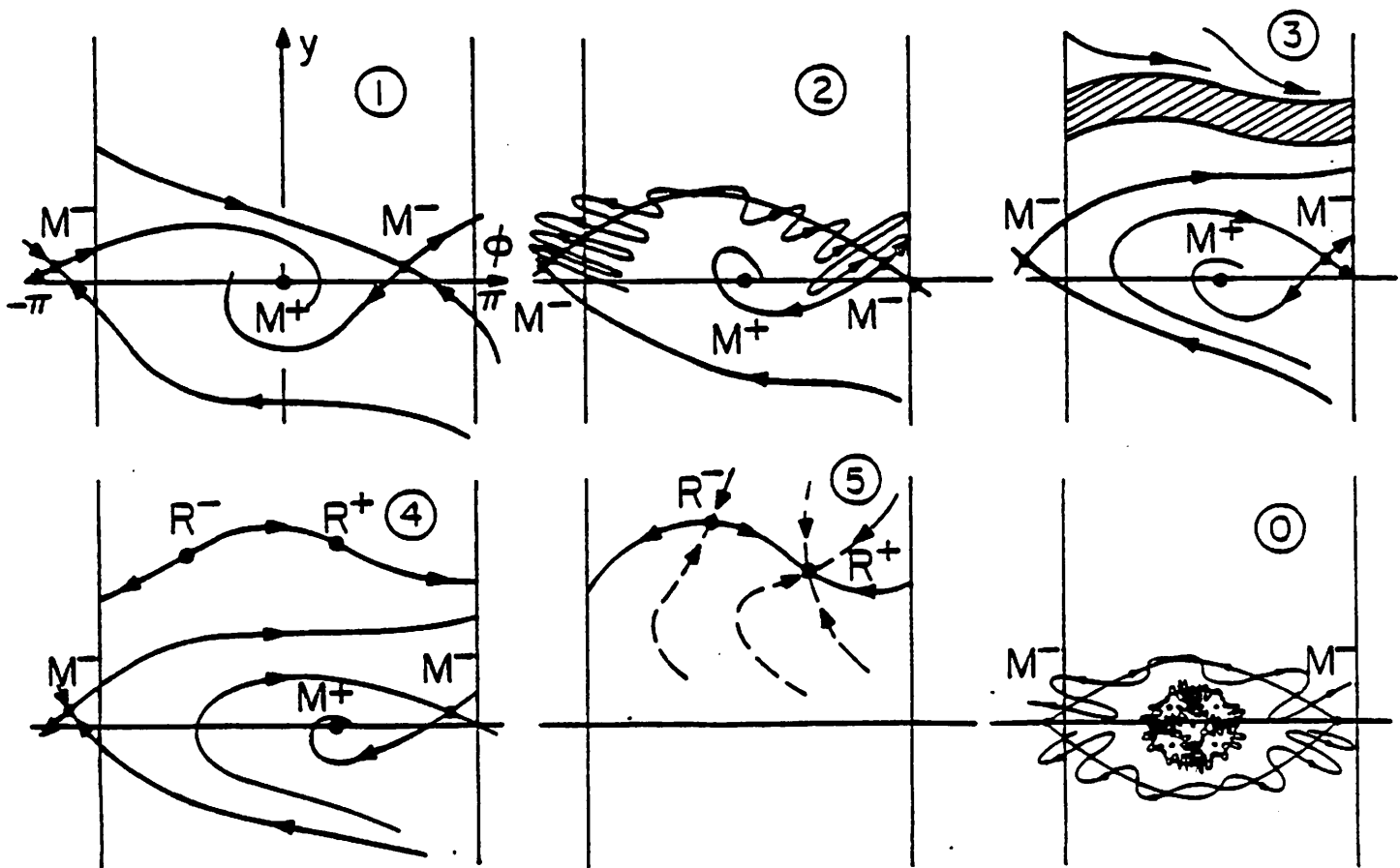
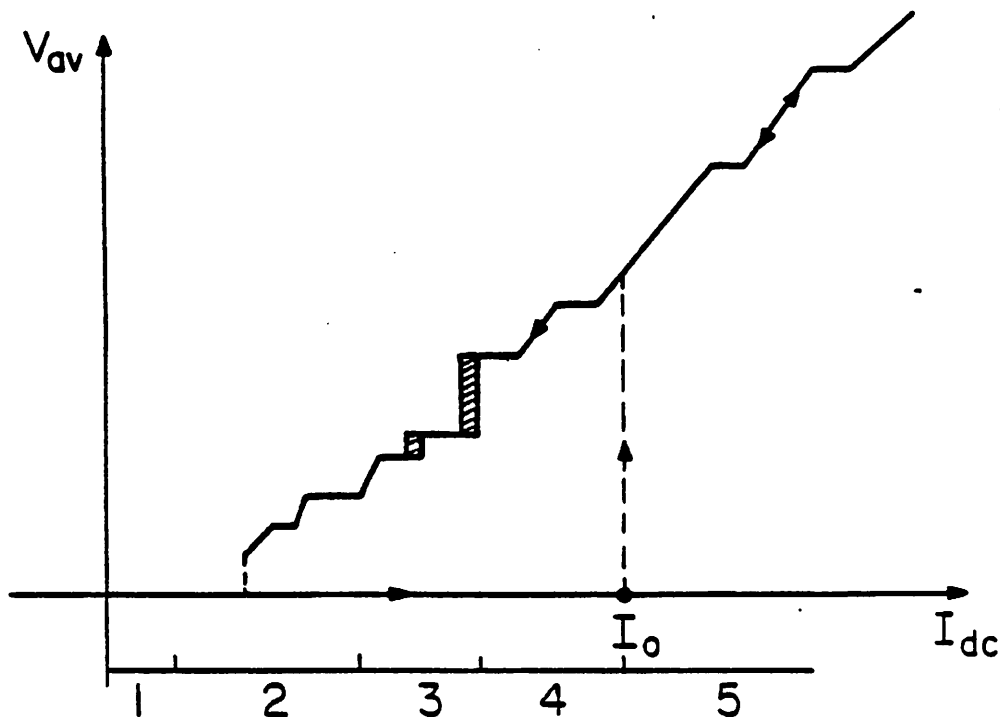


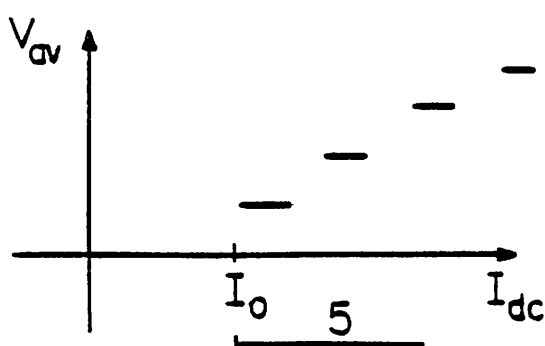
Figure 6. Portraits of the Poincaré map for different regions of Fig. 5



(a)

Figure 7a. I-V characteristic of an ac forced Josephson junction from [7].

On the I_{dc} axis the extent of the regions 1,2,3,4,5 of Figure 5
are shown.



(b)

Figure 7b. Showing stepwise discontinuous and piecewise constant characteristic in region 5

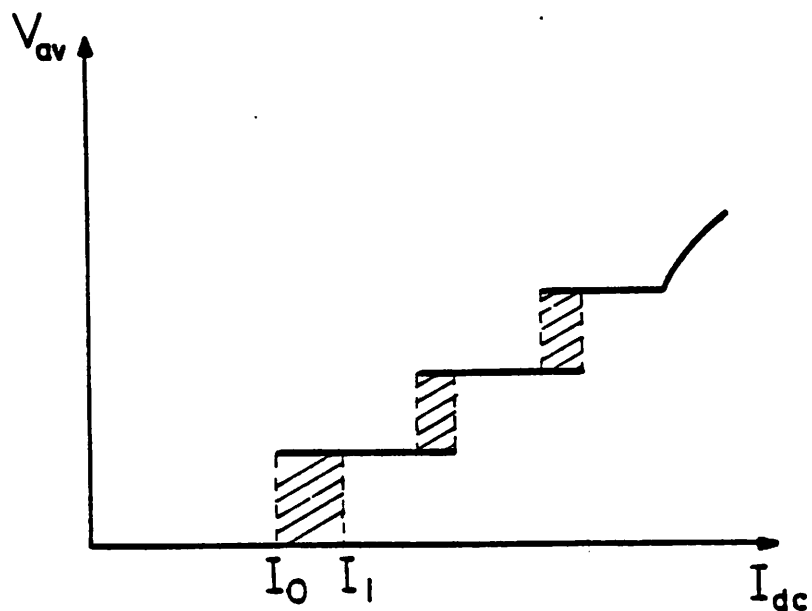


Figure 7c. Shaded regions in the V_{av} - I_{dc} curve of [6].

Chaos was observed via simulations for $\rho = 0.7155$, $\beta = 8.5$.

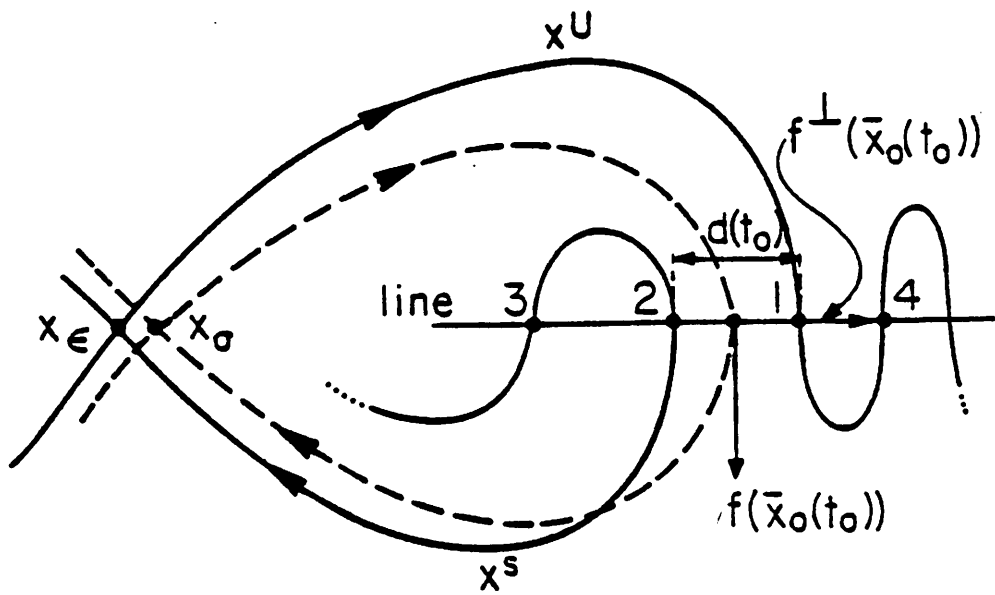


Figure 8. Showing the perturbation of the homoclinic orbit and the definition of $d(t_0)$

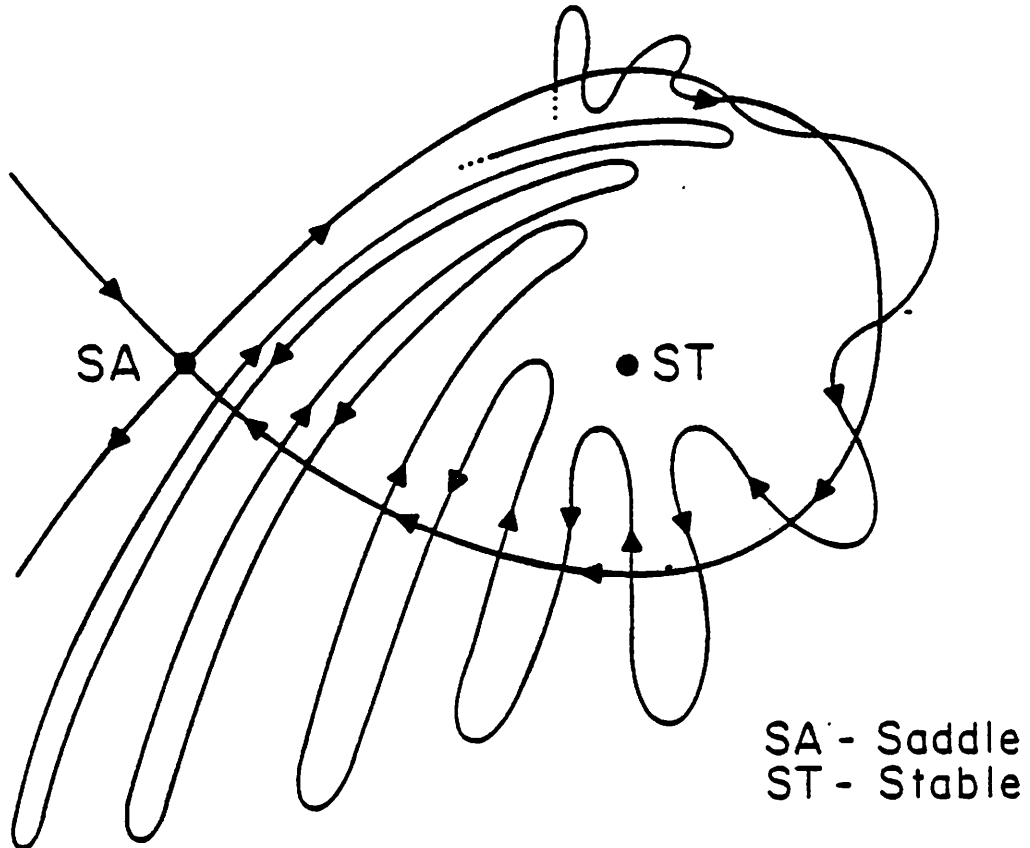


Figure 9. The Poincare map of a perturbed homoclinic orbit showing infinitely many intersections of the stable and unstable manifolds

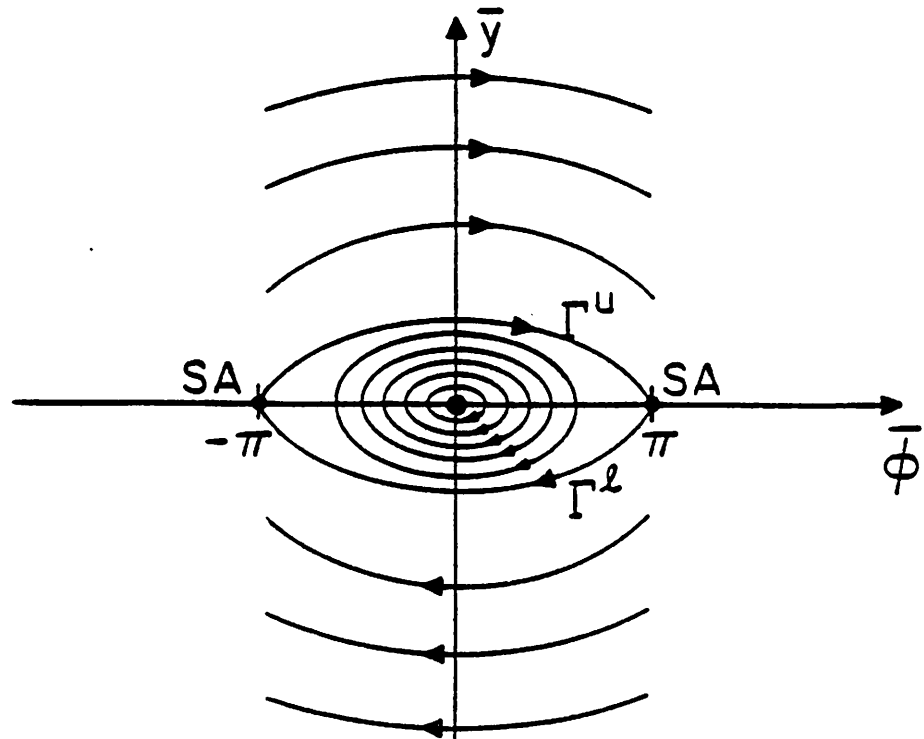


Figure 10. Phase portraits of the unperturbed unforced Hamiltonian system

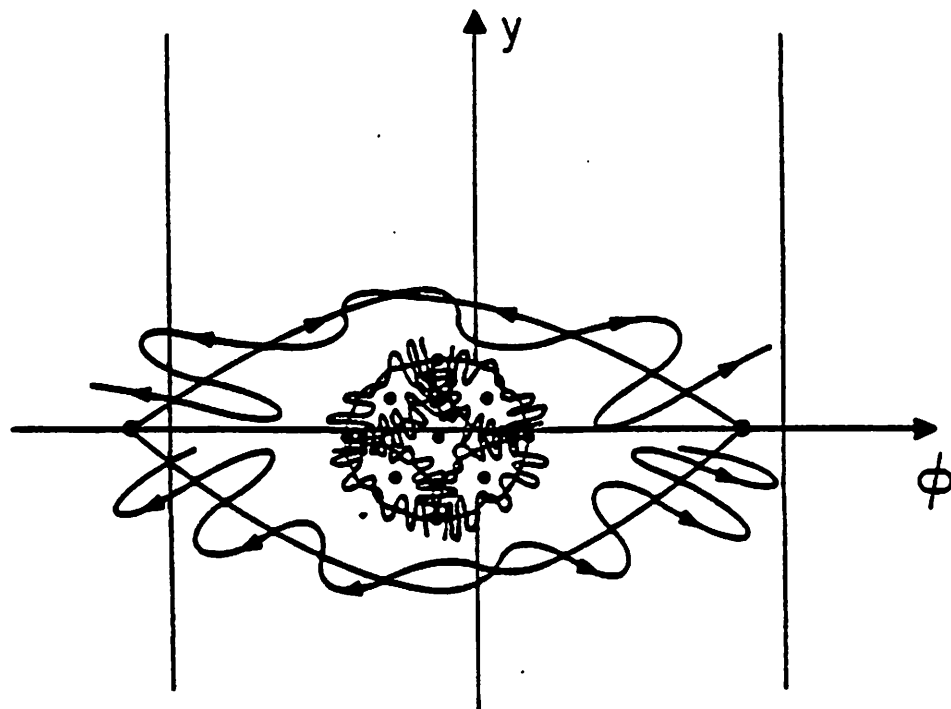


Figure 11. Small periodic perturbation of the Hamiltonian system of Fig. 10-- corresponding to the junction with high and intermediate values of β .

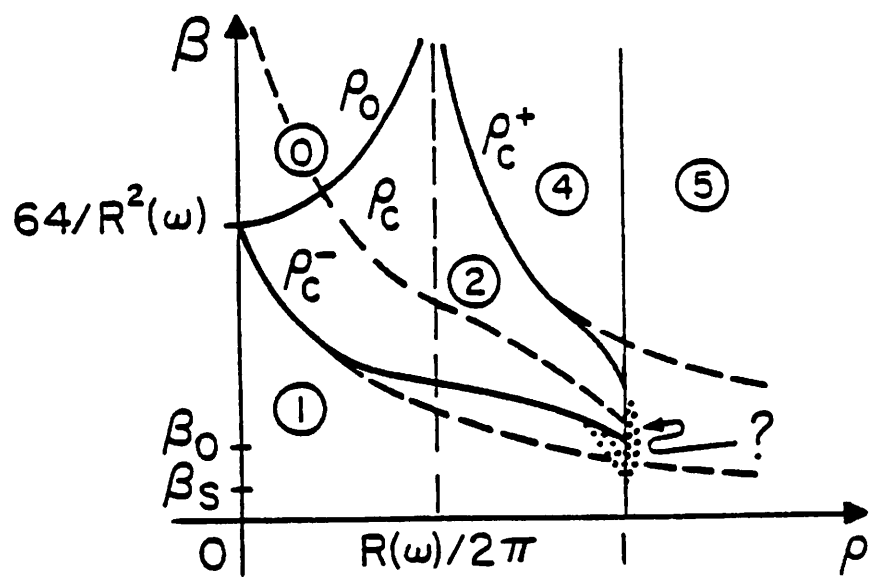


Figure 12. The bifurcation diagram of system (2.9) when $\gamma = 0$